



# 1 **Leveraging leaf-level optimality processes with explicit acclimation** 2 **improves global GPP representation in an individual-based DGVM** 3 **(LPJ-GUESS v4.1.1)**

4 Matthew Forrest<sup>1</sup>, Mateus Dantas de Paula<sup>1</sup>, Filipe Gomes de Almeida<sup>2</sup>, Sandy P. Harrison<sup>3</sup>, I. Colin  
5 Prentice<sup>4</sup>, Thomas Hickler<sup>1,5</sup>

6 <sup>1</sup> Senckenberg Biodiversity and Climate Research Centre (SBiK-F), Senckenberg – Leibniz Institution for Biodiversity and  
7 Earth System Research, Frankfurt, Germany

8 <sup>2</sup> Department of Earth and Environmental Sciences, Lund University, Lund, Sweden

9 <sup>3</sup> Geography and Environmental Science, University of Reading, Reading, United Kingdom

10 <sup>4</sup> Georgina Mace Centre for the Living Planet, Department of Life Sciences, Imperial College London, Silwood Park Campus,  
11 London, United Kingdom

12 <sup>5</sup> Department of Physical Geography, Johann Wolfgang Goethe University of Frankfurt, Frankfurt, Germany

13

14 *Correspondence to:* Matthew Forrest ([matthew.forrest@senckenberg.de](mailto:matthew.forrest@senckenberg.de))

15 **Abstract.** Vegetation models are indispensable tools for investigating and projecting the terrestrial carbon cycle, both as  
16 standalone models and embedded in global climate models. However, current models vary widely in their representation of  
17 ecosystem processes and consequently in their projected future carbon dynamics. Eco-evolutionary optimality (EEO)  
18 approaches, which derive and test hypotheses about optimal plant behaviour under specific environmental conditions as a  
19 consequence of natural selection, have been proposed as a means to improve the reliability of vegetation models and the  
20 robustness of their future projections. Here we embed EEO-derived models for photosynthesis and leaf dark respiration, and  
21 their acclimation to changing conditions, into the widely used LPJ-GUESS vegetation model. We evaluated the simulated  
22 gross primary production (GPP) patterns against remotely-sensed GPP derived from sun-induced fluorescence and found that  
23 the EEO configurations improved the spatial distributions (a mean reduction in error of 15% across gridcells) and global  
24 interannual variability (a mean reduction in error of 32% after accounting for differences in global totals) compared to the  
25 standard version of LPJ-GUESS. Evaluation against GPP fluxes from eddy flux covariance measurements also showed  
26 improved performance, the  $R^2$  of 5-day GPP increased from 0.45 to 0.48 (averaged across 147 sites). The simulated global  
27 carbon pools, fluxes, burnt area and biome distributions were not impacted substantially. The improvements were achieved  
28 with no alteration to processes except photosynthesis, respiration and plant water uptake, and with no recalibration or tuning.  
29 The EEO configuration also reduced model run time and eliminated the need for poorly-constrained PFT-dependent parameters  
30 governing the temperature response of photosynthesis. As well as being a tangible improvement to LPJ-GUESS, this study  
31 further confirms the usefulness of EEO approaches to improve global vegetation models.



## 32 1 Introduction

33

34 Aggregated terrestrial photosynthesis, known as gross primary productivity (GPP), is a major flux in the global carbon cycle  
35 (Anav et al., 2015). Only about half of the carbon fixed by photosynthesis is used to produce biomass (Collalti et al., 2020),  
36 and a large proportion of the remainder is respired to support maintenance of tissues (Atkin et al., 2015). The photosynthetic  
37 apparatus in leaves is particularly costly to maintain, and leaf maintenance respiration, also referred to as leaf mitochondrial  
38 (dark) respiration ( $R_d$ ), is estimated to use around 25% of GPP (Piao et al., 2013; Ren et al., 2024). Understanding the response  
39 of these large carbon fluxes to environmental conditions is pivotal for understanding and simulating Earth system dynamics  
40 (Lombardozzi et al., 2015), especially given the strong coupling between the atmosphere and the biosphere.

41

42 Models of the terrestrial biosphere, including dynamic global vegetation models (DGVMs) and land surface models (LSMs),  
43 typically simulate GPP and  $R_d$  as part of their terrestrial carbon cycle. Although there is some shared ancestry between such  
44 vegetation models, they make different assumptions about the mechanisms controlling GPP and  $R_d$ , and different choices about  
45 the number of plant functional types (PFTs) they use and their associated parameter values. Whilst the models usually  
46 reproduce the present day spatial patterns of GPP reasonably well, they show very divergent patterns of carbon uptake by the  
47 biosphere under future climate change projections (Arora et al., 2020) reflecting a lack of understanding of the controls on  
48 these basic processes (De Kauwe et al., 2014; Intergovernmental Panel on Climate Change (IPCC), 2023; Prentice et al., 2015).  
49 Most models simulate photosynthesis using the Farquhar, von Caemmerer and Berry (FvCB) biochemical model (Farquhar et  
50 al., 1980) or the modified version proposed by Collatz et al. (1991, 1992), both of which require three parameters:  $V_{\text{cmax}}$ , the  
51 maximum carboxylation rate;  $J_{\text{max}}$ , the maximum electron transport rate; and  $c_i:c_a$ , the ratio of leaf-internal to external  $\text{CO}_2$   
52 concentration,  $\chi$ . Although the FvCB biochemical model (or Collatz variant) is common across vegetation models, they take  
53 different approaches to defining these parameters. They also take different approaches to modelling  $R_d$ . Many models treat  
54 dark respiration as a temperature dependent process, assume that this is proportional to  $V_{\text{cmax}}$  at a fixed temperature (usually  
55  $25^\circ\text{C}$ ) and treat this as a constant per PFT and model the temperature dependence of  $R_d$  and  $V_{\text{cmax}}$  with separate Arrhenius  
56 equations (Crous et al., 2022). However, some models consider respiration as a function of the available carbon substrate pool  
57 or consider the requirements for maintenance and growth separately (Atkin et al., 2017).

58

59 Photosynthesis and dark respiration respond to environmental conditions on two different timescales. On short timescales (i.e.  
60 near instantaneous),  $V_{\text{cmax}}$ ,  $J_{\text{max}}$  and  $R_d$  respond to changes in temperature as they are governed by enzyme kinetics. Over  
61 longer timescales (days to weeks) plants optimize their photosynthetic capacities, dark respiration and stomatal behaviour to  
62 changing environmental conditions through acclimation (Kumarathunge et al., 2019; Reich et al., 2016, 2021; Smith et al.,  
63 2019; Smith and Dukes, 2013). The representation of acclimation in current vegetation models is limited. Some models do  
64 not represent thermal acclimation (e.g. Krinner et al., 2005; Niu et al., 2011), while those that do use represent thermal



65 acclimation using empirical functions and PFT-specific parameters derived from databases of plant trait measurements (Atkin  
66 et al., 2015; Kattge and Knorr, 2007) but using different timeframes ranging e.g. from the last 10 days or current monthly mean  
67 (Butler et al., 2021; Haverd et al., 2018; Huntingford et al., 2017; Mercado et al., 2018; Oliver et al., 2025; Vuichard et al.,  
68 2019). Models that include acclimation to changing temperature do not consider acclimation to other drivers such as  
69 atmospheric CO<sub>2</sub> concentration, [CO<sub>2</sub>] (Bagley et al., 2015; Sage et al., 1989; Tissue et al., 1993), radiation (Atkin et al., 1998;  
70 Ghannoum et al., 1997; Liu et al., 2024), and VPD (Li et al., 2018; Middleby et al., 2024).

71

72 The Lund-Potsdam-Jena (LPJ-) DGVM (Sitch et al., 2003) and related models like LPJ-GUESS (Smith et al. 2014) adopt a  
73 somewhat different approach for calculating  $V_{\text{cmax}}$  and  $R_d$ . In this case an optimal daily  $V_{\text{cmax}}$  is calculated based on the  
74 assumption that plants optimise the net leaf-level photosynthetic gain, i.e.  $\text{GPP} - R_d$ , for a given daily temperature, radiation,  
75 daylength and [CO<sub>2</sub>]. An additional temperature-response of photosynthesis is included according to an empirically-derived  
76 unimodal response function, with fixed (and poorly constrained) parameters for tropical, temperate and boreal PFTs (Sitch et  
77 al. 2003).  $R_d$  is linearly related to  $V_{\text{cmax}}$  so is also adjusted daily. Whilst this formulation allows plants to adjust their  
78 photosynthetic capacity and  $R_d$  according to temperature, it is not a reasonable representation of acclimation as the timescale  
79 of this adjustment (one day) is unrealistically short.

80

81 Eco-evolutionary optimality (EEO) approaches have been suggested as a means to improve the vegetation models and enable  
82 more robust predictions by improving the representation of ecosystem processes and reducing the reliance on poorly  
83 constrained parameters (Harrison et al., 2021). EEO theory assumes that processes are optimised by natural selection and  
84 proposes concrete hypotheses about plant behaviour in response to environmental conditions. EEO hypotheses focus on  
85 predicting optimal plant function given environmental conditions, whilst acknowledging that plants do not immediately  
86 achieve this optimum but rather will adjust their functioning towards the predicted optimum at an appropriate time scale - i.e.  
87 they explicitly account for acclimation. This time scale varies from days-to-weeks for ecophysiological processes, to millennia  
88 or longer for evolutionary processes. A further advantage of EEO approaches is that they are based on equations derived from  
89 hypothesised plant behaviour rather than empirical relationships, and so they are innately well-suited to represent the broad  
90 spectrum of plant behaviour and dynamic traits, without discretising vegetation into PFTs with fixed trait values.

91

92 The P-model (Prentice et al., 2014; Stocker et al., 2020; Wang et al., 2017) is a universal model of GPP which combines three  
93 EEO hypotheses (the least cost hypothesis, the coordination hypothesis and the cost-benefit hypothesis for  $J_{\text{max}}$ : see Materials  
94 and Methods) and the FvCB model of C<sub>3</sub> photosynthesis. It simulates responses of photosynthesis to temperature, solar  
95 radiation, vapour pressure deficit, [CO<sub>2</sub>] and atmospheric pressure. The standard version of the P-model (P model v1: Stocker  
96 et al., 2020) uses weekly or monthly climate inputs and so implicitly includes acclimation of ecophysiological processes on a  
97 weekly-to-monthly timescale. The sub-daily version of the P-model (Mengoli et al., 2022), which was explicitly designed for  
98 incorporation in LSMs, separates the instantaneous and acclimated response of photosynthesis to temperature where the



99 acclimated response was determined from noontime conditions over a period of ~15 days (Mengoli et al., 2022). A similar  
100 acclimation timescale has been identified for leaf dark respiration (Ren et al., 2024). Ren et al. (2025) have incorporated both  
101 the sub-daily P-model and an EEO-based scheme for  $R_d$  that represents the adjustment of leaf respiration to nighttime  
102 temperature and the coupling of  $V_{cmax}$  with canopy level  $R_d$  into the Noah-MP LSM. They showed that overestimation of GPP  
103 (10%) and canopy respiration (200%) in the standard version of the Noah-MP model compared to observed values at eddy  
104 covariance flux sites was substantially reduced (GPP: 2% overestimation; canopy respiration: 8% overestimation), pointing to  
105 the utility of adopting these schemes in vegetation models.

106 In this study we test the applicability of EEO-derived representations of leaf-level processes, including explicit representation  
107 of acclimation, in LPJ-GUESS (Smith et al., 2001, 2014). LPJ-GUESS is a widely-used, community-developed DGVM, which  
108 has also been implemented as an LSM in a number of climate models (Döscher et al., 2022; Forrest et al., 2020; Weiss et al.,  
109 2014). Our focus here is to go beyond the site-scale study with prescribed absorbed radiation and vegetation types of the  
110 Noah-MP study global implementation (Ren et al. 2025) by testing globally and with fully prognostically calculated light  
111 absorption and simulated vegetation dynamics. Specifically we (i) implemented the P-model and a complementary  
112 representation of leaf dark respiration in LPJ-GUESS, (ii) compared the simulated global GPP with a remotely-sensed GPP  
113 product based on sun-induced fluorescence (SIF), (iii) compared simulated GPP with measurements from eddy flux covariance  
114 sites and (iv) evaluated the effects of the new implementation on simulated global carbon pools and fluxes, water fluxes and  
115 the distribution of vegetation types.

## 116 **2 Materials and methods**

### 117 **2.1 LPJ-GUESS (Lund-Potsdam-Jena General EcoSystem Simulator)**

118 LPJ-GUESS (Smith et al., 2001, 2014) integrates processes ranging from ecophysiology and tree population dynamics to  
119 biogeochemical cycles, global vegetation biome changes, disturbances by wildfires and (in specific versions, not here) land  
120 use. The processes described in this section are enabled for all simulations presented here, unless specifically mentioned as  
121 modified or disabled for the EEO version of the model. Vegetation dynamics are simulated as the emergent outcome of growth  
122 and competition for light, space and soil resources (here nitrogen and water) among woody plant individuals and a herbaceous  
123 understorey in each of a number of replicate patches representing ‘random samples’ of each simulated locality or grid cell.  
124 Multiple patches are simulated to account for the distribution within a landscape representative of the grid cell as a whole of  
125 vegetation stands differing in their histories of disturbance and stand development (succession). The simulated plants are  
126 classified into one of a number of Plant Functional Types (PFTs) discriminated by growth form, phenology, photosynthetic  
127 pathway (C3 or C4), bioclimatic limits for establishment and survival and, for woody PFTs, allometry and life history strategy.  
128 These traits determine which PFT competes most successfully in a given environment and, thereby, the relative cover of each  
129 PFT. Here we used the standard global PFTs set with ten tree PFTs and two herbaceous PFTs following Smith et al. (2014).



130

131 LPJ-GUESS's existing photosynthesis scheme follows the approach of LPJ-DGVM (Sitch et al. 2003), with the addition of a  
132 nitrogen limitation on photosynthetic rates following (Smith et al., 2014). Canopy fluxes of CO<sub>2</sub> and water vapour are  
133 calculated by a coupled photosynthesis and stomatal conductance scheme based on the approach of BIOME3 (Haxeltine and  
134 Prentice, 1996a, b). The scheme first calculates optimal photosynthesis in the absence of water stress by calculating the  $V_{\text{cmax}}$   
135 which maximises net photosynthesis after accounting for leaf mitochondrial respiration (i.e. GPP -  $R_d$ ) assuming fully open  
136 stomata i.e.  $\chi = \chi_{\text{max}} = 0.8$ .  $R_d$  is calculated as a fixed fraction of  $V_{\text{cmax}}$ . This  $V_{\text{cmax}}$  is used to calculate the unstressed  
137 photosynthesis and the corresponding transpirational water demand (via the requisite canopy conductance and the Priestly-  
138 Taylor representation of evapotranspiration). This demand is then compared to the water supply through roots from the soil  
139 to determine if the plant is water stressed. If this is the case, and the canopy conductance is down-regulated until the demand  
140 matches the supply, which also reduces  $\chi$  and photosynthesis. Water supply here was calculated using LPJ-GUESS's default  
141 water update take scheme (referred to as "ROOTDIST") which calculates supply as the product of plant root-distribution-  
142 weighted soil moisture and a maximum transpiration rate (5 mm day<sup>-1</sup>). In this water uptake scheme, plant water availability  
143 is not limited by soil moisture content until the wilting point is reached, at which point available water is zero.

144

145 Nitrogen limitation is introduced to LPJ-GUES's standard photosynthesis calculation as a scalar on  $V_{\text{cmax}}$  before any  
146 consideration of water stress (i.e. at the calculation of unstressed photosynthesis above). The scalar is the ratio of current  
147 photosynthetically-active leaf N content to the optimal leaf nitrogen. The latter is calculated based on unstressed  $V_{\text{cmax}}$   
148 following (Haxeltine and Prentice, 1996a) and the former depends on soil N availability and the individual's uptake strength  
149 which depends on root surface area (Smith et al., 2014).

150

151 After subtracting respiration costs, the net primary production (NPP) accrued by an individual woody plant or the herbaceous  
152 layer each simulation year is allocated to leaves, fine roots and, for woody PFTs, sapwood, following a set of allometric  
153 relationships for each PFT, resulting in biomass, height and diameter growth (Sitch et al., 2003). Population dynamics  
154 (recruitment and mortality) are represented as stochastic processes, influenced by current resource status, demography and the  
155 life history characteristics of each PFT (Hickler et al., 2004). In the global standard version here, vegetation-stand-destroying  
156 disturbances are simulated as a stochastic process, affecting individual vegetation patches with an expectation of 0.01 yr<sup>-1</sup>,  
157 which very roughly mimics natural disturbances such as tree diseases, storms and bark beetle attacks. In addition, wildfires are  
158 modelled prognostically using the SIMFIRE model (Knorr et al., 2014) with fire emissions and mortality calculated with the  
159 BLAZE model (Rabin et al., 2017) and are enabled in all simulations presented here. Litter arising from phenological turnover,  
160 mortality and disturbances enters the soil decomposition cycle. The carbon and nitrogen soil decomposition dynamics are  
161 jointly simulated using a scheme adapted from the CENTURY model (Parton et al., 1993). The soil hydrology scheme follows  
162 Gerten et al. (2004) which includes interception, infiltration, and percolation, and was recently updated to use 15 soil layers  
163 (Zhou et al., 2024).



164

## 165 2.2 The P-model

166 The P-model v1.0 (Stocker et al., 2020) combines an optimality-derived light-use efficiency (LUE) prediction with the  
167 Farquhar–von Caemmerer–Berry model for C<sub>3</sub> photosynthesis (FvCB). The LUE prediction is based on three EEO hypotheses.  
168 The Coordination Hypothesis (Chen et al., 1993; Haxeltine and Prentice, 1996a; Maire et al., 2012) assumes that plants equalise  
169 their RuBisCo-limited rate of photosynthesis ( $V_{\text{cmax}}$ ) and their electron-transport limited rate of photosynthesis (limited by both  
170  $J_{\text{max}}$ , the maximum rate of electron transport, and absorbed light) under growth conditions on a weekly-to-monthly timescale  
171 to optimise the use of available light. The Least Cost Hypothesis (Prentice et al., 2014) states that plants minimise the sum of  
172 the costs per unit assimilation for maintaining their apparatus for photosynthesis and transpiration. The Cost-Benefit  
173 Hypothesis for  $J_{\text{max}}$  (Peng et al., 2020; Wang et al., 2017) posits that plants optimise their  $J_{\text{max}}$  so as to maximise the net benefit  
174 i.e. the benefit to their assimilation rate minus the cost of maintaining their electron transport chain. Predictions for  $V_{\text{cmax}}$ ,  $J_{\text{max}}$ ,  
175 and  $\chi$  (the ratio of leaf intercellular CO<sub>2</sub> concentration to atmospheric CO<sub>2</sub> concentration) are derived from these assumptions  
176 and used to calculate gross assimilation rates using the FvCB model (Stocker et al., 2020; Wang et al., 2017). The P-model  
177 v1.0 also includes a temperature-dependent quantum yield of photosynthesis,  $\varphi_0$ , and an empirical soil moisture limitation  
178 factor which was calibrated from a subset of the globally available eddy flux covariance measurement sites (Stocker et al.,  
179 2020). The model calculates LUE on a monthly timestep (to implicitly account for acclimation assuming an acclimation time  
180 scale of one month) but calculates photosynthesis on a finer timestep, with both daily and 8-day averages giving similar results.  
181 Cai and Prentice (2020) extended the P-model to include C<sub>4</sub> photosynthesising plants by accounting for their increased LUE  
182 due to their CO<sub>2</sub> concentrating mechanism at the cost of a lower  $\varphi_0$ . The model was further developed by Mengoli et al. (2022)  
183 to calculate photosynthesis on a subdaily time step and to explicitly account for acclimation with an acclimation period of  
184 approximately 15 days.

185

186 The P-model as implemented in this study takes the v1.0 model as a starting point (including the temperate-dependent  $\varphi_0$  and  
187 the empirical soil moisture stress function) and also includes the extension for C<sub>4</sub> photosynthesis and the explicit 15-day  
188 acclimation period from (Mengoli et al., 2022) in place of the implicit monthly acclimation used in (Stocker et al., 2020).  
189 However, as LPJ-GUESS uses daily mean values for climate inputs, we do not implement the full subdaily P-model. Instead,  
190 we use daily mean values both for acclimation and for the calculation of GPP. Thus the model presented here is a hybrid  
191 between the P-model v1.0 (Stocker et al., 2020) and the subdaily P-model (Mengoli et al., 2022), with the additional  
192 approximation that plants acclimate to daily mean conditions.

193

194 Conceptually, GPP is calculated as the product of light use efficiency and absorbed photosynthetically active radiation ( $I_{\text{abs}}$ ):

195

$$196 \quad GPP = I_{\text{abs}} \cdot LUE$$

(1)



197

198 Where  $I_{abs}$  is in turn calculated the product of incoming solar radiation (PAR, mol s<sup>-1</sup> m<sup>-2</sup>), the fraction absorbed of PAR  
199 absorbed by a vegetation (fAPAR, dimensionless) and the canopy-to-leaf scaling parameter,  $\alpha_a$  (dimensionless), which  
200 accounts for inefficiencies in the canopy absorption of PAR (i.e. losses due to absorption by woody tissues and gap in the  
201 canopy)

202

$$203 \quad I_{abs} = PAR \cdot fAPAR \cdot \alpha_a \quad (2)$$

204

205 However, in LPJ-GUESS photosynthesis is calculated per individual and in terms of  $A_{indiv}$  (mol s<sup>-1</sup> m<sup>-2</sup>), the assimilation rate  
206 of a vegetation individual. We therefore define

207

$$208 \quad I_{abs,indiv} = PAR \cdot fAPAR_{indiv} \cdot \alpha_a \quad (3)$$

209

210 where  $fAPAR_{indiv}$  is calculated following LPJ-GUESS's standard light interception scheme (Smith et al., 2001) and GPP (gC  
211 m<sup>-2</sup> day<sup>-1</sup>) of an individual for one day is defined as

212

$$213 \quad GPP_{indiv} = A_{indiv} \cdot C_{mass} \cdot daylength \quad (4)$$

214

215 here  $C_{mass}$  is the molar mass of carbon and daylength is the number of seconds in day. Grid cell total GPP is the sum of all  
216 GPP<sub>indiv</sub>.

217

218 To calculate  $A_{indiv}$  we require acclimated values for  $V_{cmax}$ ,  $J_{max}$  and  $\xi$ . This requires first calculating daily optimal values (which  
219 we denote  $V_{cmax,opt}$ ,  $J_{max,opt}$  and  $\xi_{opt}$ ) via the P-model based on the daily temperature ( $T$ ), vapour pressure deficit ( $D$ ), and  
220 atmospheric pressure ( $p$ ). These optimal values are done separately for C<sub>3</sub> and C<sub>4</sub> photosynthesis but apply to all vegetation  
221 individuals of a given photosynthesis pathway as all individuals are assumed to experience the same daily  $T$ ,  $D$  and  $p$ .

222

223 The ratio of leaf-internal to ambient CO<sub>2</sub> concentration,  $\chi$ , also represented as  $c_i:c_a$ , where  $c_i$  is the leaf internal CO<sub>2</sub> partial  
224 pressure and  $c_a$  is the atmospheric CO<sub>2</sub> partial pressure (calculated as  $c_a = [CO_2] \cdot p \cdot 10^{-6}$ ) is predicted as:

$$225 \quad \chi_{opt} = \frac{\Gamma^*}{c_a} + \left(1 - \frac{\Gamma^*}{c_a}\right) \cdot \frac{\xi_{opt}}{\xi_{opt} + \sqrt{D}} \quad (5)$$

226 and where

$$227 \quad \xi_{opt} = \sqrt{\frac{\beta \cdot (K + \Gamma^*)}{1.6 \cdot \eta^*}} \quad (6)$$

228



229 where  $\beta$  is the ratio of carboxylation to transpiration cost 25 °C, taken as a globally-fitted constant value of 146 for C<sub>3</sub>  
230 photosynthesis (Stocker et al., 2020) and 146/9 for C<sub>4</sub> photosynthesis (Bernacchi et al., 2001);  $K(T)$  is the effective Michaelis-  
231 Menten coefficient for Rubisco kinetics (See Appendix A1);  $\Gamma^*(T, p)$  is the photorespiratory point in the absence of dark  
232 respiration (See Appendix A2); and  $\eta^*(T, p)$  is the correction factor for the viscosity of water relative to its value at 25 °C  
233 calculated following (Huber et al., 2009).

234

235 Daily optimal  $V_{cmax}$  and  $J_{max}$  ( $V_{cmax,opt}$  and  $J_{max,opt}$ ) are calculated based on Mengoli et al. (2022, their equations 1 and 2) but  
236 on a per unit  $I_{abs}$  basis (so  $I_{abs}$  removed) and refactored in terms of  $m_C$  and  $m_J$  defined as:

237

$$238 \quad m_C = \frac{\chi_{opt} - \Gamma}{\chi_{opt} + \kappa} \quad (7)$$

$$239 \quad m_J = \frac{\chi_{opt} - \Gamma}{\chi_{opt} + 2\Gamma} \quad (8)$$

240  $\Gamma = \Gamma^*/c_a$  and  $\kappa = K/c_a$  for convenience. Defining via  $m_C$  and  $m_J$  allows us to conveniently adopt the approximation that for  
241 C4 photosynthesis  $m_C = m_J = 1$  following (Cai and Prentice, 2020).

242

243 Thus

$$244 \quad V_{cmax,opt} = \frac{\varphi_0 \sqrt{m_J^2 - c^{*2/3} \cdot m_J^{4/3}}}{m_C} \quad (9)$$

$$245 \quad J_{max,opt} = \frac{4 \cdot \varphi_0}{\sqrt{1 / \left\{ 1 - \left( \frac{c^*}{m_J} \right)^{2/3} \right\} - 1}} \quad (10)$$

246 where  $c^*$  is a cost factor estimated to be 0.41 (Wang et al., 2017) and  $\varphi_0(T)$  is the temperature-dependent quantum yield for  
247 photosynthesis which differs for C3 and C4 photosynthesis (see Appendix A3). Under conditions of very high  $T$  and  $D$ , the  
248 square root term in equation (10) yields an imaginary number; in this case all photosynthesis rates are set to zero.

249

250 The values are then standardised to 25 °C:

251

$$252 \quad V_{cmax25,opt} = V_{cmax,opt} / f_V(T) \quad (11)$$

$$253 \quad J_{max25,opt} = J_{max,opt} / f_J(T) \quad (12)$$

254

255 where  $f_J(T)$  and  $f_V(T)$  are Arrhenius functions (see Appendix A4) with activation energies of 71513 J mol<sup>-1</sup> and 49884 J mol<sup>-1</sup>  
256 for  $V_{cmax}$  and  $J_{max}$  respectively.

257



258 To acclimate these values for day,  $d$ , we apply the weighted-mean method with  $\alpha = 0.067$  which corresponds to an acclimation  
259 time of approximately 15 days (Mengoli et al., 2022). These must be calculated on a per-individual basis because individuals  
260 intercept different  $I_{abs}$  and so values are scaled by their specific  $I_{abs,indiv}$ . We use the *indiv* subscript to indicate values that are  
261 both acclimated and specific to a vegetation individual, the *acclim* subscript indicates quantities that are acclimated but are  
262 common to all vegetation individuals (but still depends on their photosynthetic pathway). In full:

$$263 V_{cmax25,indiv}^d = (1.0 - \alpha) \cdot V_{cmax25,indiv}^{d-1} + I_{abs,indiv} \cdot \alpha \cdot V_{cmax25,opt} \quad (13)$$

$$264 J_{max25,indiv}^d = (1.0 - \alpha) \cdot J_{max25,indiv}^{d-1} + I_{abs,indiv} \cdot \alpha \cdot J_{max25,opt} \quad (14)$$

$$265 \xi_{acclim}^d = (1.0 - \alpha) \cdot \xi_{acclim}^{d-1} + \alpha \cdot \xi_{opt}^d \quad (15)$$

267

268 The standardised values at 25 °C are then scaled back to the daily temperature to give rates for that individual for that day,

269

$$270 V_{cmax,indiv} = V_{cmax25,indiv}^d \cdot f_V(T) \quad (16)$$

$$271 J_{max,indiv} = J_{max25,indiv}^d \cdot f_J(T) \quad (17)$$

272 (dropping the superscript  $d$  for convenience)

273

274 We also calculate acclimated  $\chi$ ,  $\chi_{acclim}$ , from equation (5) using  $\xi_{acclim}^d$  in place of  $\xi_{dopt}$ .

275

276 Given these acclimated values for the day, we can calculate  $A_{indiv}$  as the minimum of the the electron transport rate,  $A_{J,indiv}$ , and  
277 the carboxylation rate  $A_{C,indiv}$  (both in  $\mu\text{mol CO}_2 \text{ m}^{-2} \text{ s}^{-1}$ ) i.e.

278

$$279 A_{indiv} = \min(A_{C,indiv}, A_{J,indiv}) \quad (18)$$

280

281 where

282

$$283 A_{C,indiv} = V_{cmax,indiv} \cdot m_C \quad (19)$$

$$284 A_{J,indiv} = J \cdot m_J / 4 \quad (20)$$

285

286 and where

287

$$288 J = \frac{4 \cdot \varphi_0 \cdot I_{abs,indiv}}{\sqrt{1 + \left(\frac{4 \cdot \varphi_0 \cdot I_{abs,indiv}}{J_{max,indiv}}\right)^2}} \quad (21)$$



289

290 and  $m_J$  and  $m_C$  are calculated following equations (7) and (8) but with  $\chi_{\text{acclim}}$  in place of  $\chi_{\text{opt}}$ .

291

292 The final daily GPP values are scaled using LPJ-GUESS's soil moisture ( $\theta$ ) and the soil moisture correction ( $\beta \in [0, 1]$ )  
293 described in (Stocker et al., 2020). The correction has two relationships: The first defines the response to soil moisture as a  
294 quadratic expression below a certain threshold ( $\theta^*$ ) and 1 (i.e. no soil moisture stress) above this threshold,

295

$$296 \quad \beta = \begin{cases} q(\theta - \theta^*)^2 + 1, & \theta \leq \theta^* \\ 1, & \theta > \theta^* \end{cases} \quad (22)$$

297

298 where  $\theta^*$  is set to 0.6 globally and  $q$  is a sensitivity parameter related to the aridity regime of the location, quantified by the  
299 mean annual ratio of actual to potential evapotranspiration (AET/PET), and is defined by

300

$$301 \quad q = \frac{\beta_0 - 1}{\theta^* - \theta_0} \quad (23)$$

302 where  $\theta_0$  is 0 in the global calibration and  $\beta_0$  is given by

303

$$304 \quad \beta_0 = \widehat{a}_\theta + \widehat{b}_\theta (AET/PET) \quad (24)$$

305

306 The parameters  $\widehat{a}_\theta$  and  $\widehat{b}_\theta$  are calibratable parameters, here set to 0 and 0.685, respectively, following (Stocker et al., 2020)

307

### 308 **2.3 Leaf Dark Respiration**

309 Given that we use mean daily climate inputs in LPJ-GUESS, we cannot implement the acclimation of respiration scheme  
310 proposed by Ren et al. (2025) which considers acclimation to both daytime and nighttime temperatures. Instead we use a  
311 simpler EEO-scheme which assumes that the dark respiration rate at standard temperature (25 °C),  $R_{d,25}$ , is a constant fraction  
312 of  $V_{\text{cmax},25}$  (Wang et al., 2020). Thus,

313

$$314 \quad R_{d,25} = b_{25} \times V_{\text{cmax},25, \text{indiv}}^d \quad (25)$$

315

316 Where  $b_{25} = 0.03$  based on fits to experimental data (Wang et al., 2020).

317



318 Daily leaf dark respiration rates are calculated from  $R_{d,25}$  and the daily mean temperature using an empirical relationship from  
319 (Heskel et al., 2016),

$$320 R_d = R_{d,25} \times e^{0.1012(T-25)-0.0005(T^2-25^2)} \quad (26)$$

321

## 322 2.4 Overview of integration into LPJ-GUESS

323 All P-model and leaf respiration functions were included via a new source code module. Program control was modified using  
324 a switch use the P-model photosynthesis which also automatically uses the EEO leaf dark respiration formulation. To improve  
325 runtime efficiency by taking advantage of the parameter-sparse nature of the P-model, the P-model optimality calculation  
326 (equations (5) and (6)) was only performed once per day for  $C_3$  and once per day for  $C_4$  photosynthesis using the daily mean  
327 temperature, atmospheric pressure and VPD of that day. After scaling to a standard temperature of  $25^\circ\text{C}$ , this produced daily  
328 optimal values for  $C_3$  and  $C_4$  photosynthesis for  $V_{\text{cmax},25}$  and  $J_{\text{max},25}$  on a per unit  $I_{\text{abs}}$  basis. These daily optimal values are  
329 universal for all PFTs of a given photosynthetic pathway because the P-model has no PFT-specific parameters. However, in  
330 LPJ-GUESS, individuals have PFT-specific parameters for structural, phenological, and demographic traits which are  
331 unchanged here. This, combined with their position in the canopy, gives each individual its own daily  $I_{\text{abs}}$ . So the daily optimal  
332 values (per unit  $I_{\text{abs}}$ ) were then multiplied by the daily  $I_{\text{abs}}$  value to give a daily optimal  $V_{\text{cmax},25}$  and  $J_{\text{max},25}$  for each tree individual  
333 as well as for  $C_3$  and  $C_4$  grasses. These values were then used to calculate the acclimated values per individual following the  
334 weighted mean approach of Mengoli et al. (2022). This technical optimisation works without any loss of precision because the  
335 first use of  $I_{\text{abs}}$  is in equations (13) and (14) where it enters linearly, so optimal  $V_{\text{cmax},25}$ , and  $J_{\text{max},25}$  can be calculated universally  
336 on a per unit  $I_{\text{abs}}$  basis.

337

338 The interface for the coupling of carbon and water fluxes with the rest of LPJ-GUESS was unchanged except that the standard  
339 water uptake mechanism, which is the lower of the demand from photosynthesis and supply from the soil, was replaced such  
340 that water uptake is determined by the demand from photosynthesis after adjustment by an empirical soil water stress function  
341 from Stocker et al. (2020). This results in water uptake being fully consistent with the photosynthetic requirement without  
342 consideration of whether the governing mechanism is supply or demand as in standard LPJ-GUESS. In the extremely rare  
343 case that available soil water was insufficient to satisfy the P-model demand, photosynthesis is scaled down proportionally to  
344 the fraction of the demand satisfied by the available water. Thus, if the P-model water demand is 1.0 mm but only 0.4 mm are  
345 available in the soil, photosynthesis would be reduced to 40%. The standard water supply functionality in LPJ-GUESS was  
346 still used, however, to calculate the daily water stress to determine the phenological state of the raingreen tree PFT and grasses  
347 to ensure consistency with phenology calculations in LPJ-GUESS which were otherwise unchanged. We used the SMART  
348 water uptake scheme (Lapides et al., 2024) since this is most consistent with the EEO assumption that plants will derive water



349 from the total soil volume rather than having a PFT-specific fixed rooting distribution. The SMART scheme also produces  
350 somewhat better results than other water uptake schemes in LPJ-GUESS.

351

352 The P-model does not consider nitrogen limitation, so the nitrogen limitation of  $V_{\text{cmax}}$  of the standard version (Smith et al.,  
353 2014) was not enabled in the EEO configuration. However, the full nitrogen cycle, including soil organic matter dynamics,  
354 was enabled in the simulations to confirm that the full model code was functioning correctly after the modifications. With one  
355 exception, this nitrogen cycling does not affect the GPP calculation or vegetation functioning. The exception is that nitrogen  
356 availability does, in principle, affect the relative allocation of biomass to foliage versus fine roots (Smith et al., 2014). However  
357 this was found to be a negligible effect here, when this was disabled in the EEO simulation global GPP changed by only ~0.1%  
358 (data not shown).



	LPJ-GUESS photosynthesis based on Haxeltine and Prentice (1996)	P-model photosynthesis (this study following (Cai and Prentice, 2020; Mengoli et al., 2022; Stocker et al., 2020))	Notes
Environmental drivers	Temperature	Temperature	Daily mean air temperature in both cases
	Absorbed photosynthetically active radiation	Absorbed photosynthetically active radiation	Determined per-individual by LPJ-GUESS's fAPAR scheme in both cases.
	Atmospheric CO <sub>2</sub> partial pressure	Atmospheric CO <sub>2</sub> partial pressure	
	Soil moisture availability (multiple soil water uptake schemes available, see below)	Soil moisture availability (via a non-EEO empirical function fitted to eddy flux covariance data, see below)	
	Equilibrium evapotranspiration (EET, depends on temperature and incoming solar radiation)	Vapour pressure deficit, $D$	Original formulation does not use observed atmospheric humidity
PFT-dependent parameters	Four to control the shape of the temperature response scalar for photosynthesis.	None	LPJ-GUESS parameters are poorly constrained and in actuality only distinguish boreal, temperature and tropical responses
Global parameters	$\alpha_a$ (=0.6)	$\alpha_a$ (=0.9)	Leaf-to-canopy scaling factor, poorly constrained.
	$\chi_{\max}$ (= 0.8)	$\chi_{\max}$ (= 0.95)	Maximum $\chi$ , P-model value demonstrably more plausible (Wang et al., 2017)
	$\theta$ (= 0.7)	-	Shape parameter governing colimitation between $V_{c\max}$ and $J_{\max}$ (Haxeltine and Prentice, 1996b)
	-	$\beta$ (=146 for C <sub>3</sub> , = 146/9 for C <sub>4</sub> )	Ratio of carboxylation to transpiration cost (Stocker et al., 2020)



	-	$c^*$ (= 0.41)	Unit cost relating to maintaining $J_{\max}$ (Stocker et al., 2020)
	-	$\widehat{C}_L$ (= 0.087182)	Calibratable parameter capturing leaf absorption properties and the maximum quantum yield (Stocker et al., 2020)
Quantum yield efficiency of photosynthesis	Fixed values	Temperature dependent (Bernacchi et al., 2003)	
Acclimation	No explicit representation, plants adjust $V_{\max}$ to daily temperature and moisture availability without memory of previous days	Explicit representation of acclimation with a 15 day period (Mengoli et al., 2022)	
Temperature response of $K_O$ , $K_C$ and $\Gamma^*$	Q10 (Haxeltine and Prentice, 1996a)	Arrhenius (Bernacchi et al., 2001)	
Temperature response of $V_{\max}$ and $J_{\max}$	None needed (daily values are calculated at growth temperature)	Arrhenius (Bernacchi et al., 2001, 2003)	
Water uptake	Depends on root distribution, no dependence on soil water content until wilting point	Follows Stocker et al. (2020) empirical scheme which uses soil water content and aridity regime to modulate plant behaviour	
Nitrogen limitation	Nitrogen limitation on $V_{\max}$ (Smith et al., 2014)	No nitrogen limitation	Nitrogen availability depends on many uncertain processes and parameters.

360

361 **Table 1: Comparison of LPJ-GUESS’s original photosynthesis scheme with the P-model implementation of this study.**

362

## 363 2.5 Simulation setups

364 We tested two model configurations: the current LPJ-GUESS trunk version (git a3506d14, svn r14188), here referred to “LPJ-

365 GUESS Standard”, and the EEO version with both the new photosynthesis and leaf dark respiration changes, here referred to

366 as “LPJ-GUESS EEO”. Both configurations were run globally (with 30 replicate patches) and at each of the FLUXNET sites

367 (with 100 replicate patches). The FLUXNET run configurations differed from the global setting only in their use of the



368 FLUXNET climate data and, in the case of biomes with clear dominant vegetation types such as the forest and grassland  
369 biomes, restricted PFT lists to match the vegetation present at the sites (see Table A1). All simulations followed the standard  
370 LPJ-GUESS procedure which comprises a 500 years spin-up period (made from detrending and repeating the first 30 years of  
371 the climate dataset) followed by a fully transient period from 1901-2022. For the *LPJ-GUESS Standard* simulations, the first  
372 100 years was simulated without N limitation to build up N pools, and then the vegetation was killed and allowed to re-establish  
373 with N limitation enabled (Smith et al., 2014).

## 374 **2.6 Model forcing data**

### 375 **2.6.1 Global forcing data**

376 We used the current standard forcing setup for LPJ-GUESS at 0.5° spatial resolution for the global simulations. This includes  
377 meteorological forcing (daily mean 2m temperature, daily total precipitation, daily total downward shortwave solar radiation,  
378 daily atmospheric pressure, daily specific humidity, daily mean wind speed) from the CRU-JRA v2.4 climate dataset  
379 (University of East Anglia Climatic Research Unit; Harris, I.C., 2023) from 1901 to 2022. Daily mean relative humidity was  
380 calculated from atmospheric pressure, specific humidity and temperature. Vapour pressure deficit (VPD) inputs for the P-  
381 model were calculated from relative humidity, temperature and atmospheric pressure. The P-model also requires atmospheric  
382 pressure as an input. Here we used atmospheric pressure derived from elevation as opposed to the atmospheric pressure from  
383 climate dataset. This is consistent with the approach taken in the P-model development papers. The other standard LPJ-  
384 GUESS input datasets used were: CO<sub>2</sub> concentration (Friedlingstein et al., 2023); nitrogen deposition (Lamarque et al., 2013)  
385 and population density (Klein Goldewijk et al., 2010., used only for the SIMFIRE fire model).

### 387 **2.6.2 FLUXNET forcing data**

388 We used started with all 212 sites available in the FLUXNET2015 dataset (Pastorello et al., 2020), downloaded from the  
389 FLUXNET data portal (<https://fluxnet.org/data/download-data/>). We extracted daily climatic variables for each site, including  
390 near-surface air temperature, daily maximum and minimum temperature, wind speed, precipitation, shortwave radiation,  
391 atmospheric pressure, and relative humidity. Using the site-specific periods of record, bias correction was applied to the CRU-  
392 JRA v2.4 climate dataset for each of the climatic variables with the Python package *ibicus* (Spuler et al., 2024), following the  
393 ISIMIP3BASD (Lange, 2019) bias correction methodology. Sites with less than one year of valid data for any required climate  
394 variable were excluded, resulting in a final set of 205 sites. For each retained site, observed FLUXNET meteorological data  
395 were merged with the bias-corrected forcing time series over the overlapping period, ensuring that in situ observations were  
396 used wherever available.



## 397 2.7 Evaluation data

398 The GOSIF GPP product (Li and Xiao, 2019) was used for global evaluation of spatial patterns, interannual variability and  
399 trend. The monthly GOSIF GPP data for 2001-2022 were aggregated from 0.05° to 0.5° using simple averaging. GOSIF GPP  
400 has recently been reported to overestimate peak seasonal GPP (Chen et al., 2024) and show decreased accuracy under high  
401 temperature, low VPD and drought (Qian et al., 2024). Furthermore, asynchronicity in SIF emission and GPP has been  
402 reported (Yang et al., 2022). Since these shortcomings could introduce systematic biases in its seasonal cycle of GPP, we  
403 evaluated model skill in reproducing the seasonal cycle with daily eddy flux covariance data from the FLUXNET2015 dataset  
404 (Pastorello et al., 2020). We excluded cropland (CRO) and wetland (WET) sites since the EEO configuration does not simulate  
405 these land cover types. Open and closed shrublands (OSH and CSH respectively) were included to represent arid sites even  
406 though the global LPJ-GUESS configuration does not include shrub PFTs. Partitioning of GPP and ecosystem respiration was  
407 done using the nighttime method (Reichstein et al., 2005) and only measurement with quality control value > 0.5 used. We  
408 selected sites with at least 2 years of data in which at least 30% of the days had measurements which exceeded the > 0.5  
409 threshold. This left a total of 147 sites (see supplementary material for full list and metadata). We focused on GPP averaged  
410 over five days with the additional requirement that there were valid measurements on at least four of those days, although we  
411 also report daily and monthly values.

412  
413 To examine the effect of the EEO implementation on biome distributions globally, we used potential natural vegetation (PNV)  
414 data from Haxeltine and Prentice (1996b) and a matching biome classification scheme for LPJ-GUESS output (Smith et al.,  
415 2014). Whilst newer datasets exist (e.g. Hengl et al., 2018), the Haxeltine and Prentice (1996b) dataset, and the accompanying  
416 classification scheme, is widely used in the LPJ-GUESS community and provides a well-understood point of reference.

417  
418 GPP is linearly dependent on both light use efficiency and absorbed radiation and thus any error in fAPAR will propagate to  
419 simulated GPP. We therefore investigated the relationship between the error in simulated GPP versus GOSIF GPP and the  
420 error in simulated fAPAR versus observed fAPAR. To quantify fAPAR we selected a dataset based on AVHRR LTDR V5  
421 which has had cross-sensor calibration applied, and has been corrected for orbital drift and cloud cover and harmonized with  
422 MODIS (Jeong et al., 2024). For our calculation of the modelled fAPAR error, we used data from 2001 to 2021, temporally  
423 aggregated to single annual average values and spatially aggregated from 0.05° to 0.5° using simple averaging.

## 424 2.8 Evaluation metrics

425 For comparing spatial maps of GPP we use the normalised mean error (NME, (Kelley et al., 2013)):

$$427 \text{NME} = \frac{\sum_i |y_i - x_i|}{\sum_i |x_i - \bar{x}|} \quad (24)$$

428



429 where  $y_i$  is the modelled value in grid cell  $i$ ,  $x_i$  is the observed value and  $\bar{x}$  is the mean of the observed values across all grid  
430 cells.

431

432 As our simulations had different global total GPP, we used the “normalised mean error - step 2” (NME\_2, Kelley et al., 2013)  
433 when comparing the interannual variability of global total GPP. This metric removes the influence of the mean values by  
434 subtracting the mean values from  $y_i$  and  $x_i$  (i.e.  $x_i \rightarrow x_i - \bar{x}$  and  $y_i \rightarrow y_i - \bar{y}$  in equation (24)). The subscript  $i$  now indexes over  
435 globally summed averaged values.

436

437 When evaluating the seasonal cycle against eddy flux covariance data we used the root mean squared error (RMSE) and  
438 coefficient of determination ( $r^2$ ).

439

## 440 **3 Results**

### 441 **3.1 Spatial and temporal patterns of global GPP**

442 Both model configurations produce spatial patterns of GPP broadly consistent with the observed patterns (Fig. 1). However,  
443 the mean annual GPP simulated by *LPJ-GUESS EEO* is 131.9 Pg C  $y^{-1}$ , very similar to the GOSIF GPP estimate of 136.5  
444 Pg C  $y^{-1}$ , whereas the *LPJ-GUESS Standard* simulation has a larger annual total of 169.5 Pg C  $y^{-1}$ . The *LPJ-GUESS*  
445 *Standard* overestimated GPP in most regions of the world except in some tropical regions and very high latitudes (Fig 2.).  
446 The overall overestimation was much reduced in the *LPJ-GUESS EEO* simulation, but this configuration underestimates  
447 GPP in the tropical forests (Fig. 2). The *LPJ-GUESS EEO* configuration reduced the NME of the spatial distribution from  
448 0.48 to 0.41 compared to the *LPJ-GUESS Standard*, an error reduction of 15%. The simulated GPP vs GOSIF GPP at the  
449 grid cell level (Fig. 3) show reasonable agreement with the one-to-one line, with the *LPJ-GUESS Standard* showing slightly  
450 better fit (goodness-of-fit,  $r^2 = 0.82$ ; gradient of fitted line,  $m = 0.87$ ) than the *LPJ-GUESS EEO* simulation ( $r^2 = 0.79$ ;  $m =$   
451  $0.72$ ). However, the *LPJ-GUESS EEO* simulation has an intercept closer to zero (0.25) than the *LPJ-GUESS Standard*  
452 simulation (0.38). These comparisons show that the main improvements produced by the *LPJ-GUESS EEO* configuration  
453 are concentrated in regions with lower GPP ( $< 1 \text{ kg C m}^{-2} \text{ year}^{-1}$ ) while the underestimation of GPP by the *LPJ-GUESS EEO*  
454 configuration at high GPP values, corresponding to tropical forests, is responsible for the poorer  $r^2$  and gradient.

455

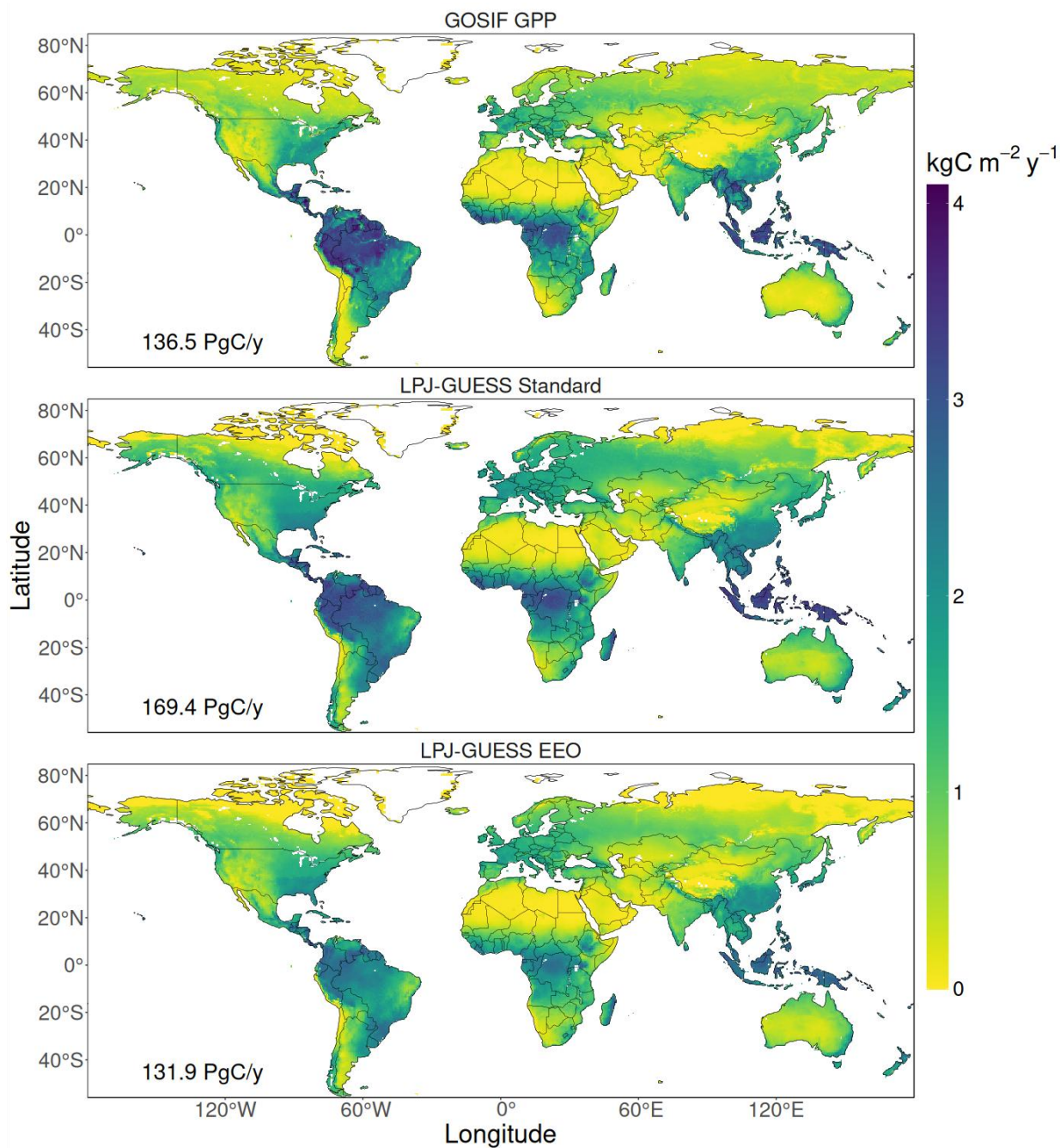
456 Given the large difference in mean total GPP between the two simulations, we compared the trend and interannual variability  
457 in global annual GPP (Fig. 4) after multiplicatively scaling the model simulations to match the first year of the GOSIF GPP  
458 data. Both configurations show an increasing trend in GPP over the last two decades, similar though slightly greater than the  
459 trend shown by GOSIF GPP. The *LPJ-GUESS EEO* simulation showed larger interannual variability than either the standard



460 configuration or the GOSIF GPP. However, quantification of model skill using the NME step 2 (NME\_2, to account for  
461 differences in the mean) shows an error improvement of 32% in *LPJ-GUESS EEO* (NME\_2 = 0.35) compared to *LPJ-GUESS*  
462 *Standard* (NME\_2 = 0.51).  
463

### 464 **3.2 Comparison to FLUXNET GPP**

465 There is small but tangible improvement in the simulation of the seasonal cycle with the EEO configuration, ( $r^2 = 0.48$ ,  
466 calculated for 5-day periods at each site and then averaged across all sites) compared to the standard configuration ( $r^2 = 0.45$ )  
467 at the 147 eddy flux covariance sites (Fig. 6, Table B2). Overall RMSE was the same for the EEO and standard configurations  
468 (both  $2.7 \text{ gC m}^{-2} \text{ day}^{-2}$ ). The EEO configuration improved the  $r^2$  fairly evenly across almost all of the IGBP-defined biomes  
469 (Fig. 6, Table B2) and improved the shape of the seasonal cycle in the seasonal forest biomes (DBF, MF, ENF) by better  
470 capturing the spring increase and the timing of peak GPP better, although underestimating the magnitude of the peak (Fig 5).  
471 The EEO configuration had a poorer  $r^2$  than the standard configuration for CSH ( $r^2 = 0.39$  compared to 0.54, Table B2), but  
472 there are only two sites and the standard configuration does not include a shrub PFT. The performance was also worse for EBF  
473 (Table 2), although this is the least well simulated biome in both configurations. Model performance was generally poorer in  
474 grassland, shrubland, and savanna biomes than in the seasonal forests (Table B2, Fig. C1).

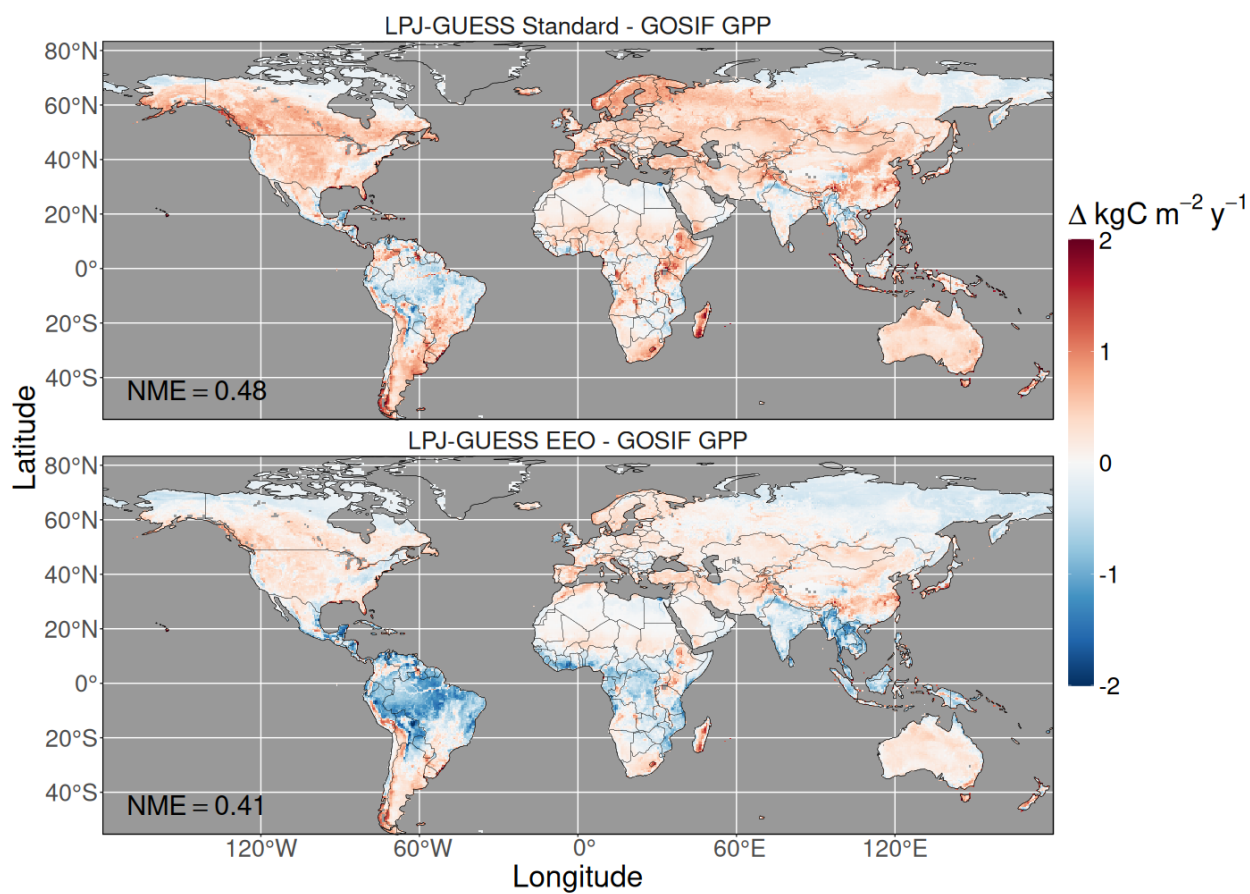


475

476 **Figure 1: Spatial distribution of mean annual GPP (2001-2022) for GOSIF GPP and the LPJ-GUESS simulations.**

477 **The inset numbers are mean annual global GPP.**

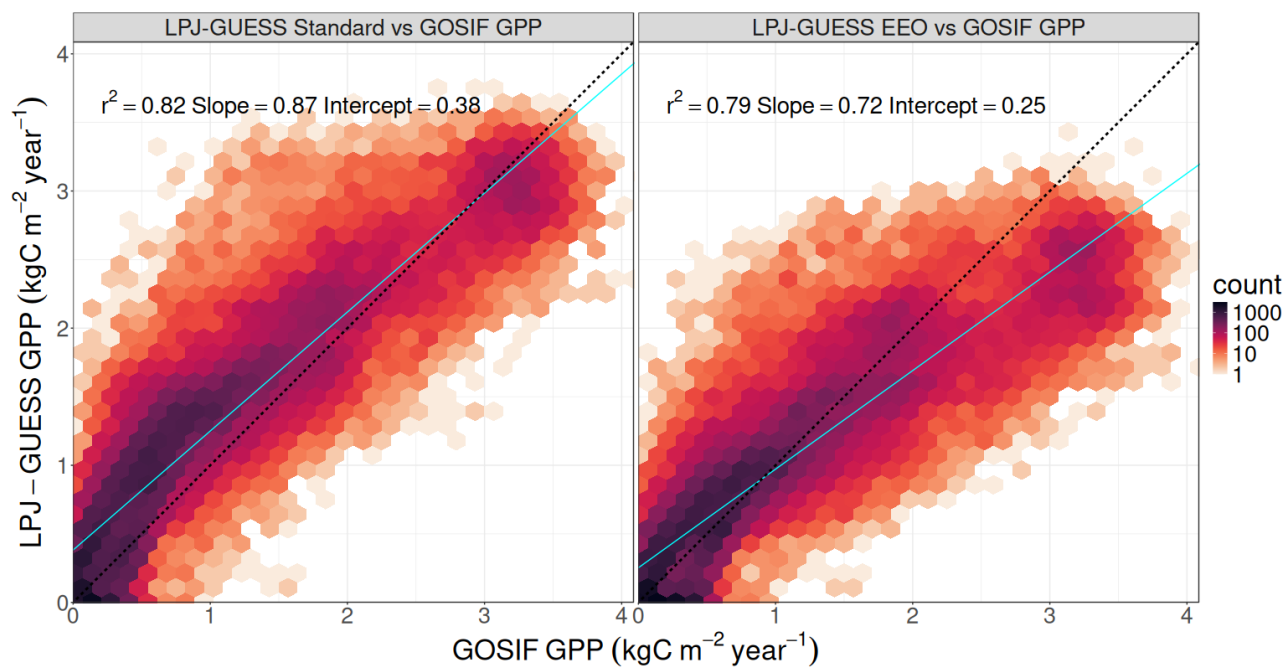
478



479

480 **Figure 2: Spatial distribution of difference in mean annual GPP (2001-2022) for the LPJ-GUESS simulations GOSIF**

481 **GPP. The inset numbers are the normalised mean errors (NME).**



482

483 **Figure 3: Scatter plot of gridcell-level mean annual simulated GPP vs GOSIF GPP (2001-2022). Black dotted lines are**  
484 **the one-to-one lines, cyan solid lines are fitted lines.**

485

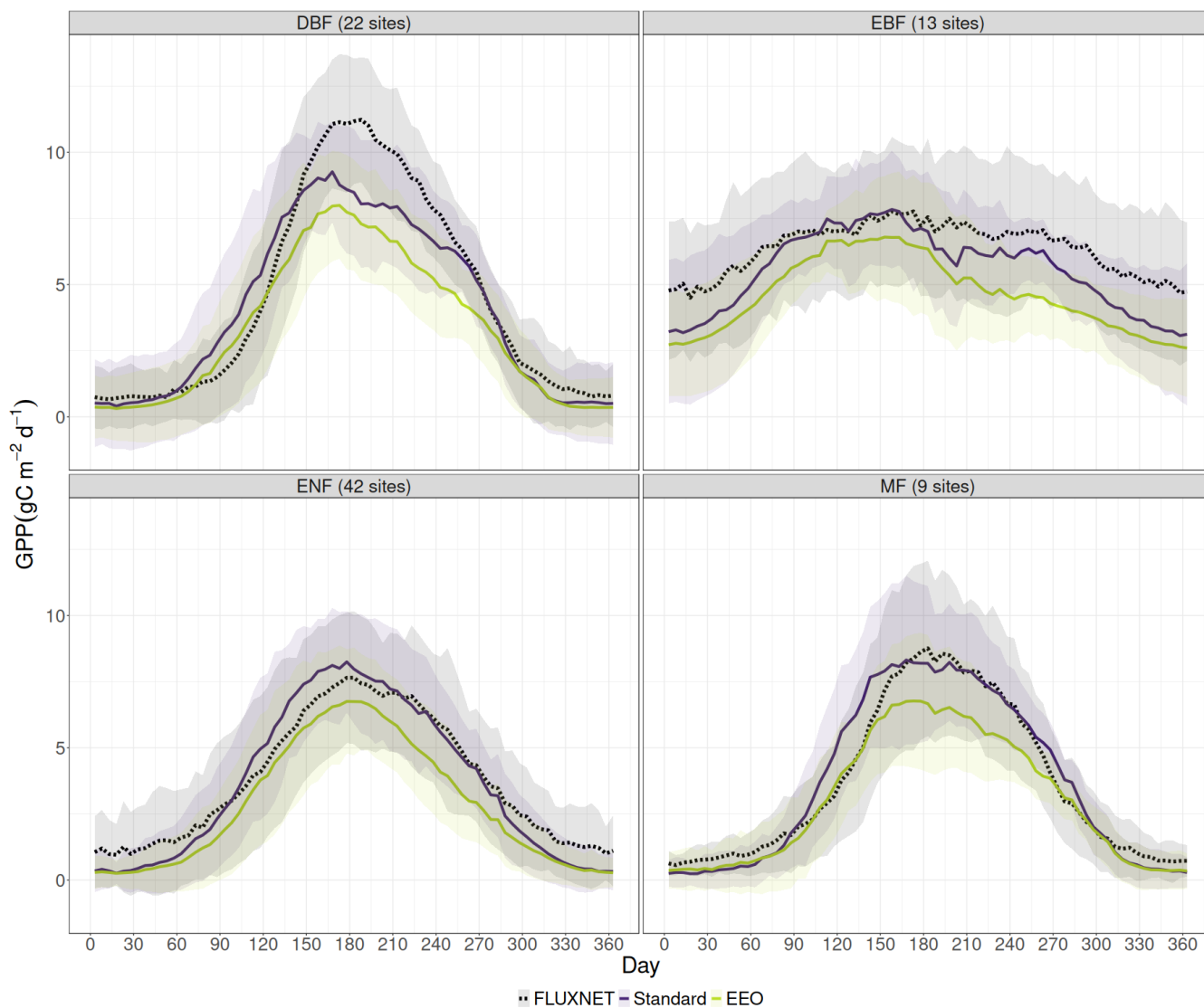


486

487 **Figure 4: Time series of mean annual GPP for the GOSIF GPP data and simulations. The simulations have been scaled**  
488 **to match the first year of the GOSIF GPP data.**

489

490



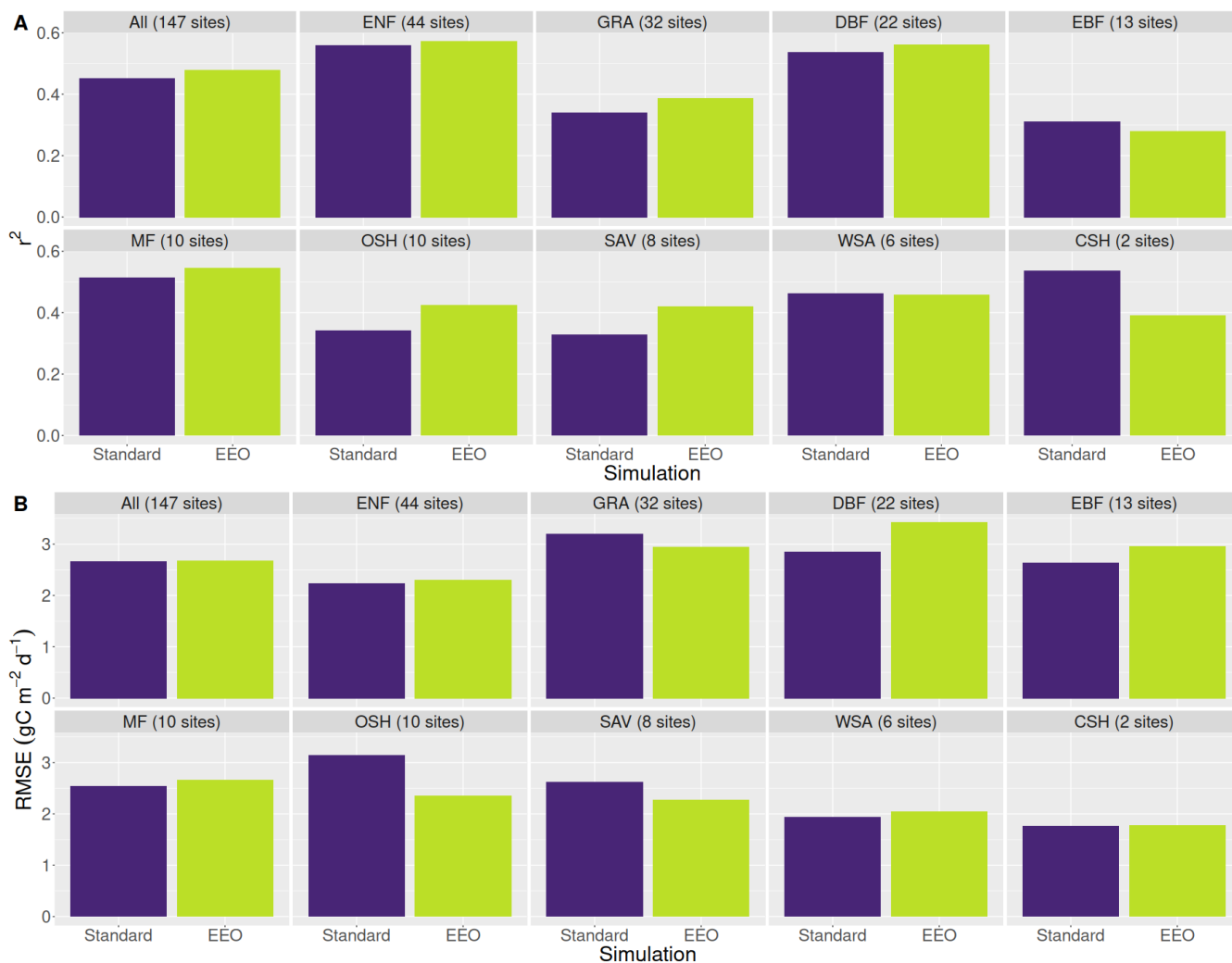
491

492

493

494

**Figure 5: Seasonal cycle of GPP from the LPJ-GUESS site simulations and the FLUXNET2015 data aggregated for deciduous broadleaf forest (DBF), evergreen broadleaved forest (EBF), evergreen needle-leaved forest (ENF) and mixed forests (MF).**



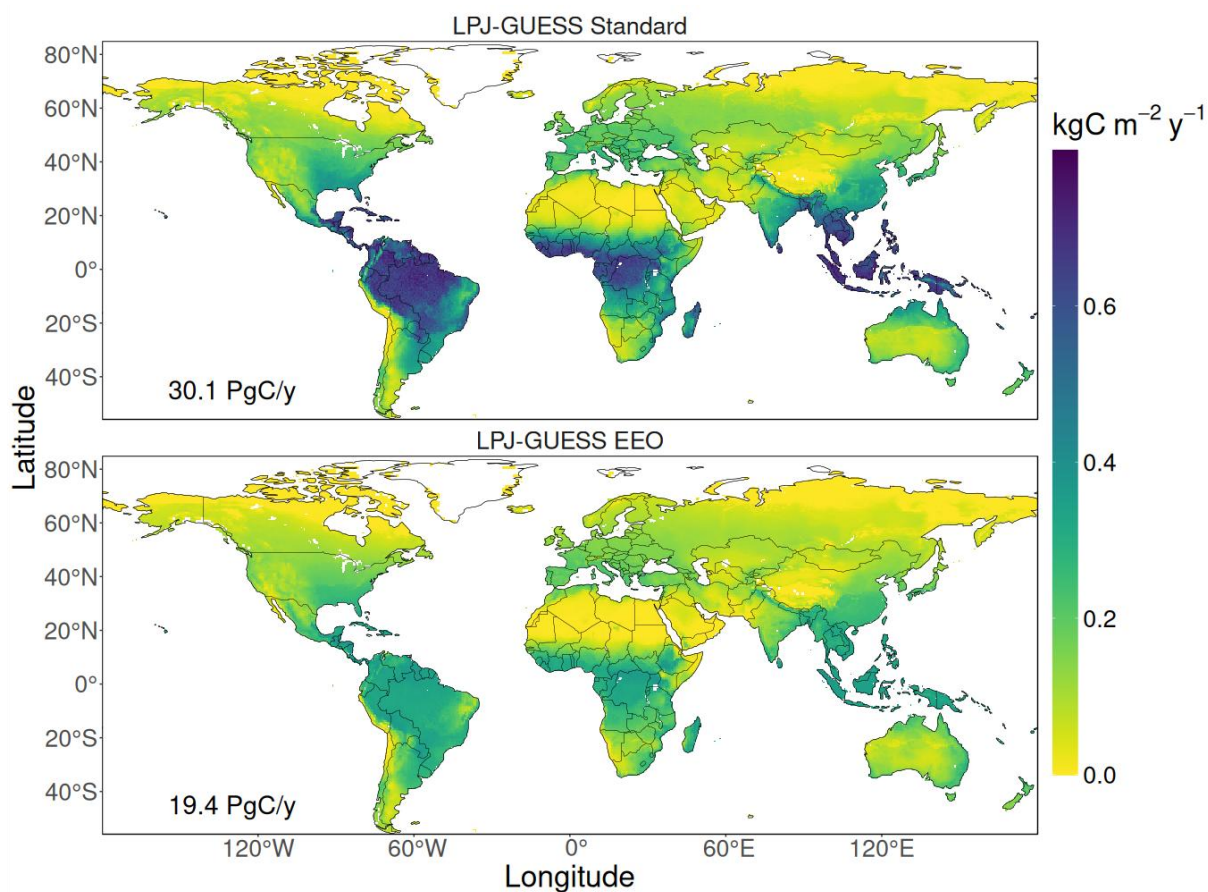
495

496

497

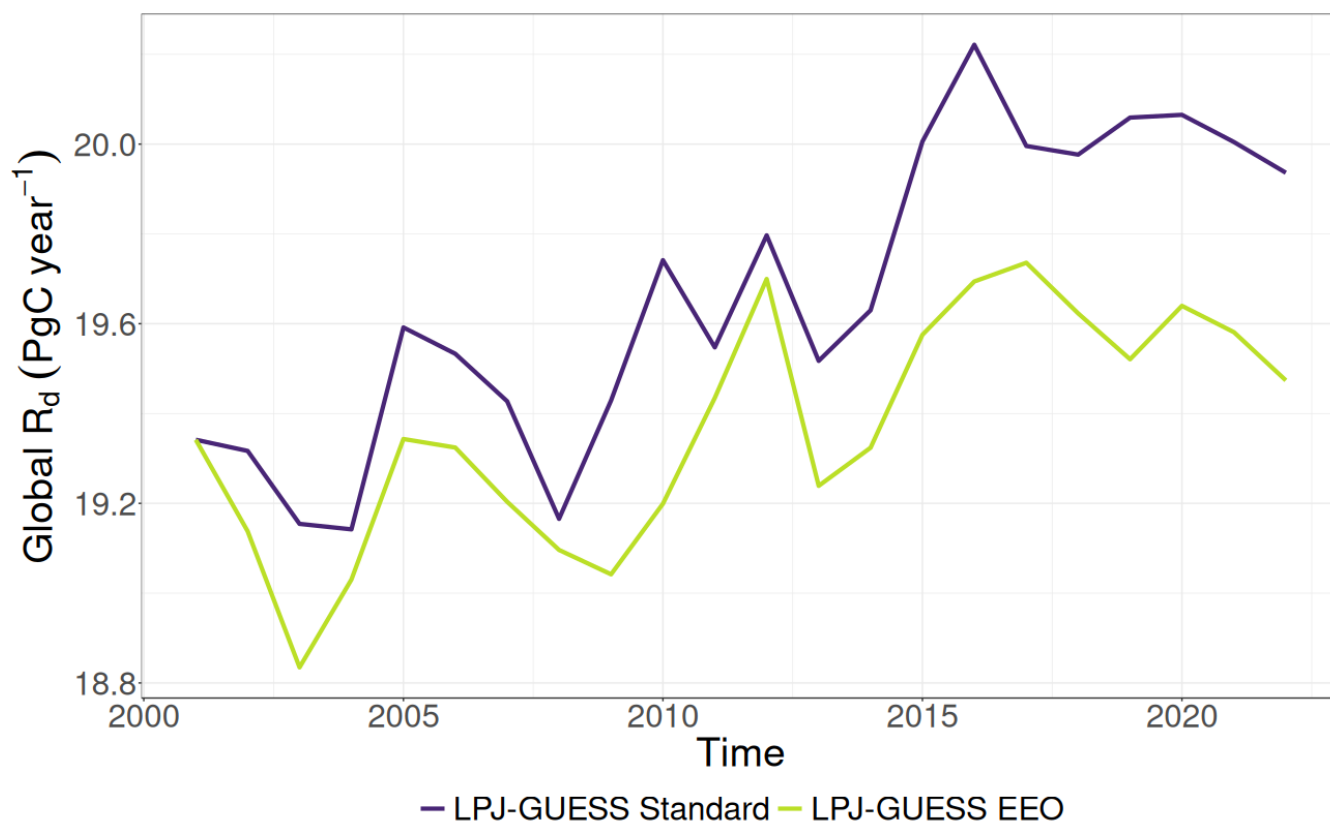
498

**Figure 6: Agreement between site-simulated LPJ-GUESS GPP and FLUXNET2015 averaged across the IGBP classified biomes as quantified by A) coefficient of determination ( $r^2$ ) and B) root mean squared error (RMSE).**



499  
500  
501  
502  
503

**Figure 7: Spatial distribution of mean annual  $R_a$  (2001-2022) for the LPJ-GUESS simulations. The inset numbers are mean annual global  $R_a$ .**



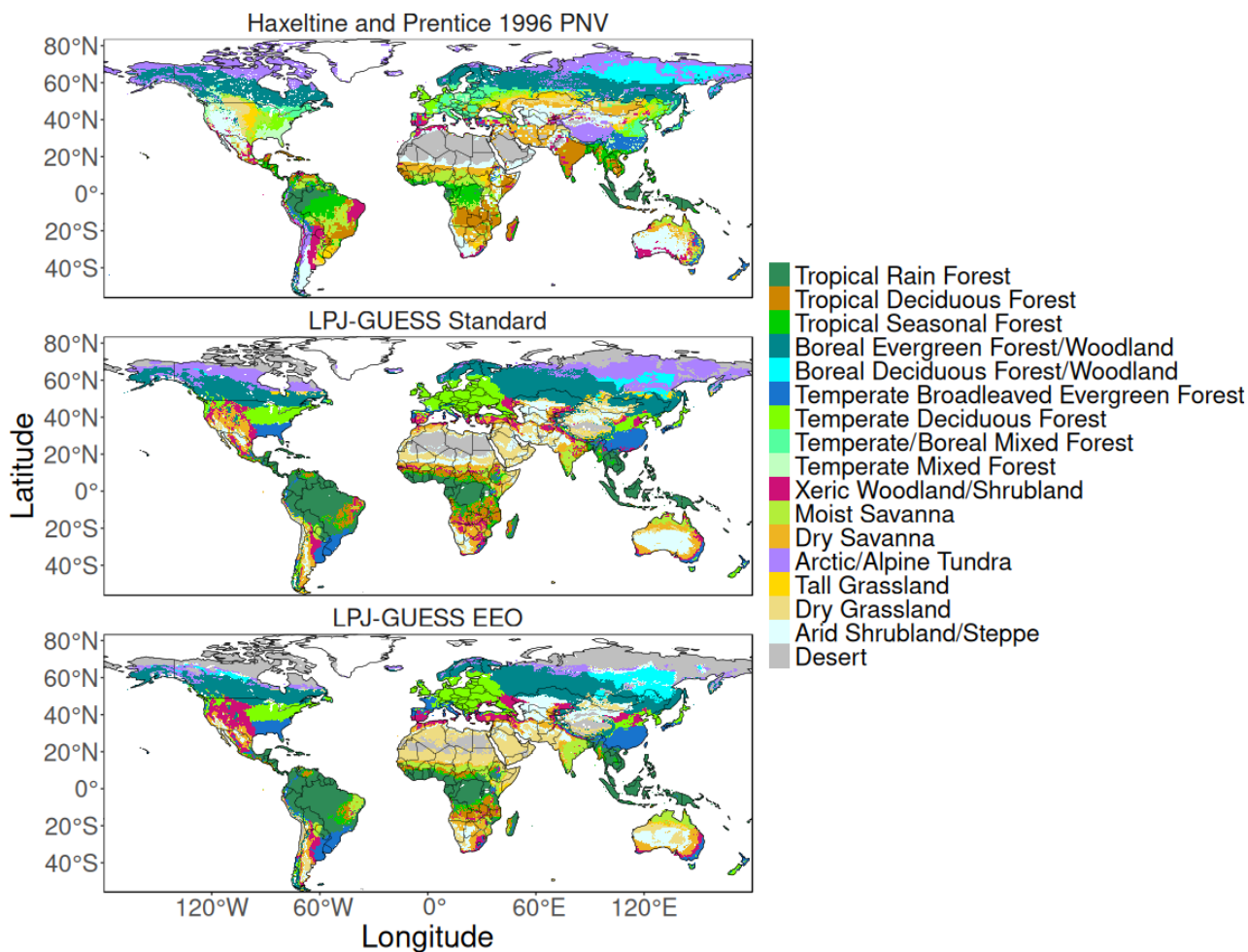
504

505

506 **Figure 8: Time series of mean annual  $R_d$  for the LPJ-GUESS simulations. The simulations have been scaled to match**  
 507 **the first year of the LPJ-GUESS EEO simulation.**

508 **3.3 Leaf dark respiration**

509 The LPJ-GUESS EEO simulation showed significantly lower  $R_d$  than the LPJ-GUESS Standard simulation (Fig. 7). This  
 510 occurred most obviously in the tropical forest regions where LPJ-GUESS EEO also underestimated GPP (Fig. 2). This  
 511 underestimation of GPP is likely to be, at least in part, due to an underestimation of  $V_{cmax}$ , which would directly cause the  
 512 underestimation in  $R_d$  observed here. The time series (Fig. 8, scaled to the starting value of the LPJ-GUESS EEO simulation),  
 513 shows the broad features expected based on the global results of (Ren et al., 2024), with  $R_d$  increasing in both simulations but  
 514 less so in the LPJ-GUESS EEO simulation due to the explicit representation of acclimation.



515

516 **Figure 9: Biome distributions simulated by both LPJ-GUESS configurations based on average LAI between 1961 and**  
 517 **1990 using the classification scheme from Smith et al. (2014) compared to a biome map from Haxeltine and Prentice**  
 518 **(1996b)**

519 **3.4 Impact on global properties**

520 The use of the EEO configuration broadly conserved the simulated global biome distributions (Fig. 9), with only 28% of the  
 521 land area changing biome. These changes are concentrated into two distinct zones (Fig. C2). The largest changes occurred at  
 522 high latitudes, with a large decrease in Arctic/Alpine Tundra which was replaced by Boreal Deciduous Forest/Woodland class  
 523 (which better matches the PNV biome map) and sharp contraction of Arctic/Alpine Tundra from the highest latitudes (in  
 524 disagreement with the PNV biomes map). There are also changes in ecotones around arid areas (e.g. the Rocky Mountains,  
 525 around the Mediterranean Sea, and seasonal tropical areas such as the Cerrado and the African savannas), where biomes  
 526 switched variously between arid shrublands and woodlands, grasslands, and savanna biomes. In the biome classification



527 scheme these biomes are distinguished by thresholds of woody and grassy LAI and the ratio between them, so changes of this  
528 nature imply shifts in tree and grass competitiveness in water-limited ecosystems. However these changes were not large  
529 enough to produce a shift from non-forest to forest biomes (Fig. 9).

530

Quantity	LPJ-GUESS Standard	LPJ-GUESS EEO	Percentage change
Total vegetation C (Pg C)	717	671	-6.4%
Total transpiration ( $\times 10^3 \text{ km}^3 \text{ H}_2\text{O y}^{-1}$ )	56.9	53.1	-6.7%
Total runoff ( $\times 10^3 \text{ km}^3 \text{ H}_2\text{O y}^{-1}$ )	37.2	39	+4.8%
Total leaf area ( $\text{Mm}^2$ )	376	347	-7.7%
Net primary productivity ( $\text{Pg C y}^{-1}$ )	62.4	60.6	-2.9%
Burnt Area ( $\text{Mha y}^{-1}$ )	230.2	232.9	+1.2%
Number vegetation individuals ( $\times 10^{12} \text{ indiv}$ )	47.0	42.0	-10.1%

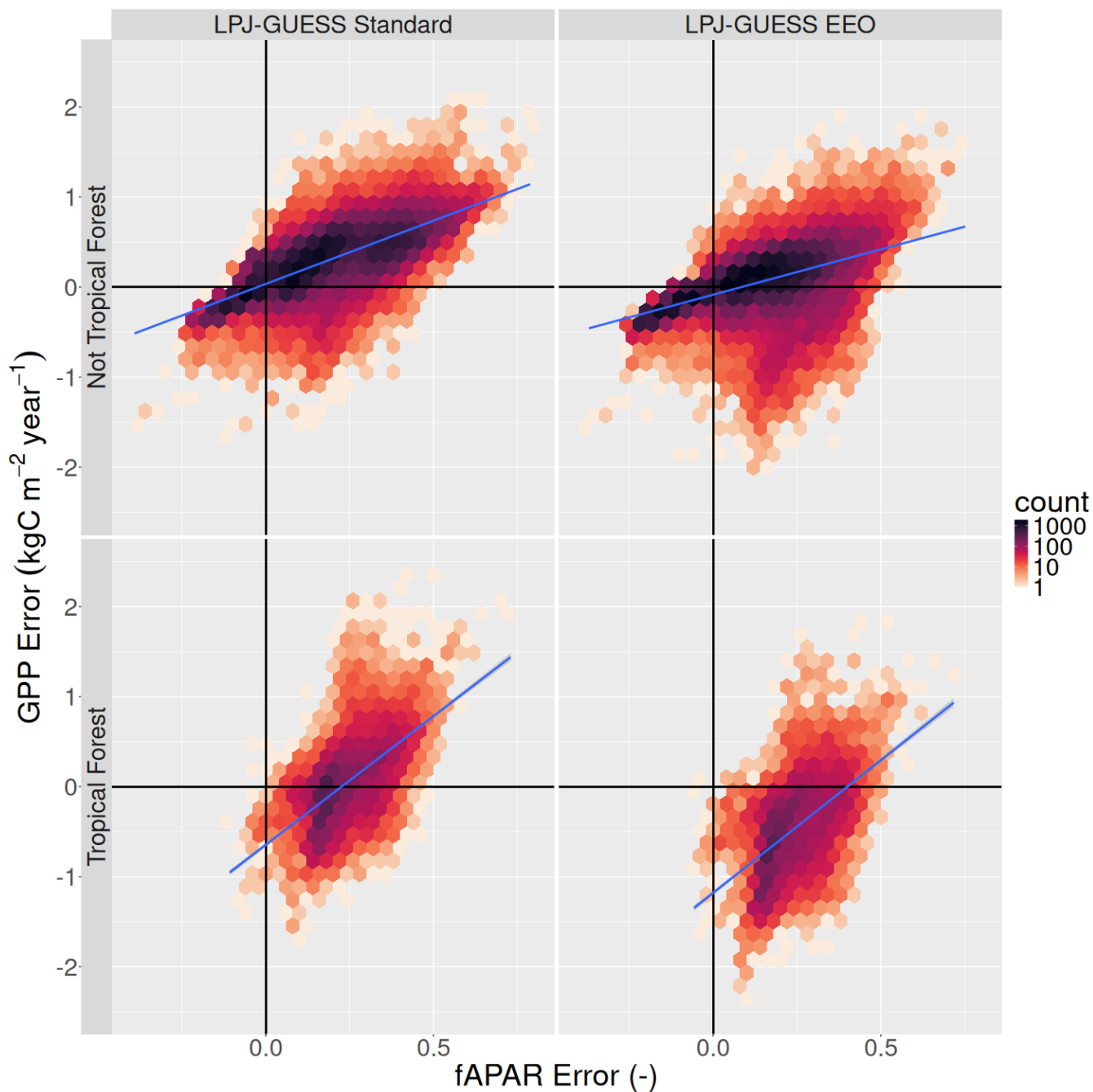
531

532 **Table 2: Global total values for LPJ-GUESS simulations (mean 2001-2020).**

533



534 Global total vegetation C, NPP, LAI, transpiration, and run-off were minimally affected by the EEO changes (Table 2). The  
535 broad picture was a little less vegetation biomass, accompanied by a reduction in transpiration and an expected, counter-  
536 balancing rise in run-off. Net primary productivity was slightly reduced by -2.9%. The total number of tree vegetation  
537 individuals (a specific property of the LPJ-GUESS model state without a direct real-world analogue) showed a reduction of  
538 10.1%, a little more than the biomass reduction and so indicated a small effect on tree demographics. Simulated burnt area was  
539 not significantly impacted as demonstrated by a small change of +1.2%.



540

541 **Figure 10: Comparison of error in simulated GPP and error in simulated fAPAR, split into tropical forest biomes and**  
542 **all other biomes (mean 2001-2022). Blue lines are fitted lines.**

543



### 544 **3.6 GPP error with respect to fAPAR error**

545 Errors in the fAPAR simulated by LPJ-GUESS will directly lead to errors in simulated GPP since we assume that GPP is  
546 linearly proportional to fAPAR. Comparison of the error in simulated GPP versus the error in simulated fAPAR on a per-  
547 biome basis showed two distinctive patterns, one in the tropical forest biomes (Tropical Rain Forest, Tropical Seasonal Forest  
548 and Tropical Deciduous Forest) and one for all other biomes (Fig. 10). In non-tropical forest biomes, the errors in GPP and  
549 fAPAR are highly correlated. The correlation of errors in the *LPJ-GUESS EEO* configuration (Pearson's  $r = 0.72$ ) is stronger  
550 than in *LPJ-GUESS Standard* configuration ( $r = 0.53$ ), but both lines of best fit pass very close the origin and most points  
551 lying in the "+ve GPP error, +ve fAPAR error" or "-ve GPP error, -ve fAPAR error" quadrants. In the tropical forest biomes,  
552 there is a tendency for both simulations to overestimate fAPAR whilst simultaneously underestimating GPP (slightly more  
553 marked in the *LPJ-GUESS EEO* simulation), resulting in steeper regression lines that did not pass close to the origin. The  
554 correlation between the errors was slightly better for *LPJ-GUESS Standard* for the tropical forest biomes compared to the  
555 other biomes ( $r = 0.58$ ), but noticeable worse for the *LPJ-GUESS EEO* simulation ( $r = 0.53$ ).

## 556 **4 Discussion**

557 The implementation of EEO hypotheses for leaf-level processes, including explicit acclimation, produced realistic results  
558 which were in general somewhat better than the original configuration of LPJ-GUESS. This implementation did not degrade  
559 the model in other respects.

### 560 **4.1 Compatibility of EEO formulations with LPJ-GUESS**

561 Overall, we found that including the EEO formulations in LPJ-GUESS produced reasonable results without the need to make  
562 major compensating changes elsewhere in the model in terms of process representations or parameter values. This indicates  
563 that the EEO formulations did not cause large disruptions in the model functioning and highlights a good degree of  
564 compatibility between LPJ-GUESS and the EEO hypotheses. There were changes in biome classification due to simulated  
565 changes in tree and grass competition, but these often occurred in areas where shrubs are an important component of the  
566 vegetation (shrubs which are not considered in the simulations). This suggests that further improvements to the simulation of  
567 arid ecosystems could be made by including a shrub PFT and refining the competition between grass and woody plants.

568  
569 The EEO formulations improved the representation of the spatiotemporal patterns of GPP at both global scale and at site level,  
570 albeit modestly. These improvements come only from adjusting the light use efficiency (and related water uptake) aspect of  
571 the GPP calculation whilst the fAPAR component is simulated using LPJ-GUESS's existing allocation, allometry, phenology,  
572 and tree population dynamics and disturbance schemes. These schemes exert a major controlling influence on GPP: allocation,  
573 allometry, and the balance between tree recruitment and mortality (in particular wildfires) govern the maximum fAPAR and  
574 therefore the maximum GPP attained in the growing season. Phenology (determined by both soil moisture and accumulated



575 temperature sums) is key in determining the seasonal development of fAPAR and hence the timing of GPP. Similarly, both  
576 LUE and fAPAR depend on available soil moisture from LPJ-GUESS's standard soil hydrology which substantially  
577 underestimate soil percolation rates under saturated conditions and therefore underestimate plant-available soil moisture  
578 (Lapides et al., 2024). These comparatively coarse and simple global representations obscure the effects of the P-model on  
579 GPP, so the fact that there are nevertheless observed improvements demonstrates the capability of the P-model to improve  
580 GPP simulation in vegetation models generally and its compatibility with LPJ-GUESS specifically.

581

582 This high level of compatibility may be due to the fact that LPJ-GUESS does not use prescribed PFT-specific  $V_{\text{cmax},25}$  unlike  
583 many other vegetation models. Instead LPJ-GUESS performs a daily calculation of  $V_{\text{cmax}}$  based on maximising GPP -  $R_d$ . This  
584 daily calculation could be considered to be a crude form of optimisation and acclimation, albeit with an unrealistically short  
585 timescale for acclimation and non-rigourously defined optimality criteria. This representation of light use efficiency in  
586 standard LPJ-GUESS was first formulated approximately three decades ago (Haxeltine and Prentice, 1996a, b) in a  
587 comparatively data-poor era. The new formulations implemented here are based on better understanding of how plants behave  
588 in a universal (i.e. PFT independent) way and more extensive evaluation than possible then, which increases confidence that  
589 the model is doing the right thing for the right reasons and thus will produce more robust future projections.

590

591 Previous applications and validations of the P-model have predicted mean responses at the ecosystem level, using either eddy  
592 flux covariance data with their implicit footprint (Mengoli et al., 2022; Ren et al., 2025) or aggregated across  $0.5^\circ$  gridcells  
593 (Cai and Prentice, 2020; Stocker et al., 2020). Here we apply a P-model variant separately to individuals in LPJ-GUESS's  
594 cohort-based vegetation state. All individuals experience the same temperature and VPD and there are no PFT specific  
595 parameters in the P-model, so the model yields the same optimal  $V_{\text{cmax}}$  and  $J_{\text{max}}$  on a per  $I_{\text{abs}}$  basis on a given day for all  
596 individuals of a given photosynthetic pathway. However, individuals experience different  $I_{\text{abs}}$  depending on their position in  
597 the canopy and their phenology and thus have different acclimated  $V_{\text{cmax}}$  and  $J_{\text{max}}$ . We have shown that this approach gives  
598 reasonable results when aggregated to the ecosystem level, implying that the P-model can be applied separately to different  
599 vegetation elements within a simulated structure. This approach also gives rise to a degree of trait/functional diversity within  
600 a modelled locality, even within a given PFT. This topic warrants further study, both in terms of a more detailed analysis of  
601 how the P-model affects vegetation structure and succession dynamics in LPJ-GUESS, and how the application of the EEO  
602 principles to different vegetation elements generates trait diversity which departs from the community means generally  
603 predicted by the theory.

#### 604 **4.2 Model performance**

605 In terms of global spatial patterns, the use of the P-model strongly reduced overestimation of GPP in extratropical areas.  
606 However, it also significantly exacerbated a small pre-existing underestimation in tropical forest areas and at high latitudes.  
607 GOSIF GPP is known to have considerable uncertainty particularly under extreme conditions, with a tendency to overestimate



608 GPP under high temperature and/or high VPD conditions (Qian et al., 2024) and peak season GPP (Chen et al., 2024) . This  
609 may be responsible for some of the apparent model underestimation in the humid tropics, but cannot explain the smaller model  
610 overestimation over much of the seasonal tropics and extratropics.

611  
612 The P-model configuration improved year-to-year interannual variability in GPP, resulting in a 32% reduction in error (even  
613 after accounting for differences in the mean values). The evaluations using eddy flux covariance measurements showed the  
614 EEO configuration improved the representation of the seasonal cycle of GPP in almost all biomes, although it underestimated  
615 peak summer values in the EBF, DBF, MF and SAV biomes. The P-model predicts a decline in light use efficiency with  
616 increasing temperatures (beyond 20°C) which is not supported by observations (Bloomfield et al., 2023) which may be  
617 responsible for this discrepancy. The P-model configuration reduced the positive bias during the spring green up. Nevertheless,  
618 there is still a bias; this is a known issue with the P-model (Stocker et al., 2020). The GPP scores were lower those found by  
619 Ren et al. (2024) and Mengoli et al. (2022). This is to be expected as the configuration tested here used a fully prognostic  
620 framework rather than prescribing fAPAR, leaf area index or soil moisture. which introduces additional model error. It also  
621 only used daily mean rather than subdaily inputs and so does not resolve the diurnal cycle of photosynthesis.

622  
623 The high correlation between GPP error and fAPAR error in most biomes (i.e. excluding tropical forests) is revealing as it  
624 implies that much of the error in GPP is not due to the error in light use efficiency calculation but rather from the fAPAR  
625 calculation. This is particularly encouraging for the P-model as in most biomes it showed notably higher correlation than  
626 standard LPJ-GUESS.

627  
628 The biggest weakness of the EEO setup is the strong underestimation of GPP in tropical forest biomes. We also found the  
629 relationship between the errors in GPP and the error in fAPAR to be different in the tropical forests compared to the other  
630 biomes. The lines of best fit were steeper and did not pass through the origin, and many of the points were in the “positive  
631 fAPAR error, negative GPP error” quadrant, indicating that even if fAPAR was perfectly simulated, GPP would be  
632 considerably underestimated, particularly by the EEO configuration. This implies that something different is going on in the  
633 tropical forests, particularly when using the P-model. One possible cause of the underestimation is that both the formulation  
634 of P-model and the calculation of fAPAR in LPJ-GESS use the Big Leaf approximation (Sellers et al., 1992) which doesn't  
635 account for diffuse radiation. Plants are believed to make more effective use of diffuse radiation, especially in dense canopies  
636 through which it can better penetrate (Gu et al., 2003), thus potentially causing the underestimation in tropical forests. Another  
637 possible cause is the previously noted decline in light use efficiency at higher temperatures; this will likely strongly impact the  
638 tropical forests results. The use of daily climate data may also be a contributing factor.

639  
640 Another area where the EEO configuration falls short is the very high latitudes where it underestimates GPP and therefore also  
641 the extent of the tundra, although the standard configuration shows the same behaviour to a lesser degree. In this case the



642 underestimation can be attributed to the lack of vegetation adapted to extreme conditions (resulting in very short growing  
643 seasons) in LPJ-GUESS's standard global PFT set. Other models with more focus on the tundra vegetation, such as BIOME4  
644 (Kaplan et al., 2003b), include arctic-focused evergreen shrub types and deciduous PFTs with lower accumulated heat sum  
645 requirements (which allows them to respond more rapidly to spring warming and so better take advantage of the short growing  
646 season), as does an arctic wetland and methane focussed version of LPJ-GUESS (Miller and Smith, 2012; Wolf et al., 2008).

### 647 **4.3 Effects of acclimation**

648 There is no indication of a large effect of long-term acclimation to changing climate and [CO<sub>2</sub>] on GPP which would cause the  
649 two LPJ-GUESS simulations to diverge. This may be because standard LPJ-GUESS does not rely on fixed per-PFT values for  
650  $V_{\text{cmax},25}$  and already includes a daily optimisation of  $V_{\text{cmax}}$  which depends on temperature and [CO<sub>2</sub>]. This is a form of  
651 acclimation, albeit an unrealistically fast one. However, the inclusion of explicit acclimation may be playing a role in the  
652 reduction of the positive bias in the northern hemisphere spring seen in the eddy flux covariance comparisons. The simulations  
653 did show a larger effect of acclimation on  $R_d$ , as the *LPJ-GUESS EEO* simulations showed less than half of the increase over  
654 2001-2022 than the *LPJ-GUESS Standard* simulation in relative terms. In comparison to the global results of Ren et al. (2024)  
655 all features are somewhat muted; with lower  $R_d$  in the *LPJ-GUESS EEO* simulation than their equivalent *H3* hypothesis results  
656 (particularly in the tropics), a smaller increase in overall in  $R_d$ , and a smaller difference between the EEO and non-EEO times  
657 series. As  $R_{d,25}$  is linked to  $V_{\text{cmax},25}$ , these differences are likely due, at least in part, to the underestimation of GPP in tropics.  
658

### 659 **4.4 Other advantages of the EEO configuration in LPJ-GUESS**

660 In addition to improvements in model skill, the EEO configuration provides other scientific and technical benefits. One key  
661 advantage is the reduced reliance on poorly-constrained parameter values and process representations. There are four poorly-  
662 constrained PFT-specific parameters in the standard LPJ-GUESS which control the shape of the temperature response of  
663 photosynthesis. Furthermore, these parameters are fixed, which limits the capacity of photosynthesis to acclimate to changing  
664 temperature. These parameters are not used in the P-model configuration. There are also global parameters which are set to  
665 more plausible values when using the P-model. The most important is  $\alpha_a$ , a canopy-to-leaf scaling parameter that accounts for  
666 inefficiencies in plant canopies that cause reductions in PAR utilisation, such as absorption by non-photosynthetic material,  
667 leaf clumping, and gaps in the canopy. The standard LPJ-GUESS uses a value of  $\alpha_a = 0.6$ , which implies that plants lose 40%  
668 of the potential radiation they could collect due to canopy inefficiencies. The value of 0.95 used in the P-model simulations  
669 appears more plausible. The value of 0.95 was an initial guess at a reasonable value and was found to produce reasonable  
670 global GPP, but could be further tuned or constrained in future applications. The P-model implementation also sets a maximum  
671 value of  $\chi$  ( $\chi_{\text{max}}$ ) of 0.95, whereas the default LPJ-GUESS value is 0.8. Values of  $\chi > 0.8$  are not uncommon (Wang et al.,  
672 2017), thus the P-model value is more plausible.



673

674 The standard LPJ-GUESS has four water uptake schemes but there is no clear rationale for choosing one over the others. The  
675 current default choice for global simulations (“ROOTDIST”) calculates water uptake based on soil water and root profile  
676 distribution but does not take soil water content into account until plant-available soil water is zero, and so allows the plants  
677 to transpire soil water without restriction until it is fully depleted. Two model choices reduce water uptake before plant-  
678 available soil water reaches zero, but the parameters have not been derived from observational data. In contrast, the soil  
679 moisture stress function used in the P-model configuration was empirically derived from observations (Stocker et al., 2020).  
680 Thus, a further benefit of the EEO configuration is to replace an unconstrained model formulation by a formulation that has  
681 been calibrated and validated against eddy flux covariance data.

682

683 The EEO configuration also has technical advantages. Model runtime was reduced by ~22% for global simulations. This is  
684 partly a consequence of the reduced number of vegetation individuals being simulated (~10%), which also has the added  
685 benefit of reducing the RAM footprint of the model. The remaining runtime reduction was due to the avoidance of the iterative  
686 numerical solver routine that standard LPJ-GUESS uses to account for water stress by finding a value of  $\chi$  that simultaneously  
687 balances the transpiration required for photosynthesis and the water uptake possible from the soil. In the *LPJ-GUESS EEO*  
688 configuration the photosynthesis-transpiration calculations take a much smaller share of the runtime.

#### 689 **4.5 Consideration of nutrient limitation**

690 One fundamental change introduced by the P-model is that photosynthetic rates are no longer directly affected by nutrient  
691 availability as they are in standard LPJ-GUESS, whereby  $V_{\text{cmax}}$  is a function of leaf active N (Smith et al. 2014), or by active  
692 N and active P in the case of a phosphorus-enabled version (Dantas de Paula et al., 2025). The inclusion of nutrient cycling  
693 and the effects of nutrient availability on  $V_{\text{cmax}}$  has been considered as a significant achievement of vegetation models,  
694 including in LPJ-GUESS (Dantas de Paula et al., 2025; Smith et al., 2014). However, although correlations between  $V_{\text{cmax}}$ , as  
695 well as  $J_{\text{max}}$ , with leaf N and P have been observed in global datasets (Walker et al., 2014), there is little evidence supporting  
696 a direct causal relationship that soil N controls  $V_{\text{cmax}}$  at the global scale. Recent meta-analyses have shown no relationship  
697 between soil N and  $V_{\text{cmax},25}$  at the community level (Peng et al., 2021) and no increase in  $V_{\text{cmax}}$  under N fertilisation (Stocker  
698 et al., 2025). This is not to say that nutrient availability is not important. The study of (Peng et al., 2021) did find a relationship  
699 between soil phosphorous and photosynthetic capacity. The study of (Stocker et al., 2025) showed that increasing N  
700 fertilisation causes increased investment in leaves, and therefore increases GPP via by increasing fAPAR. Furthermore, they  
701 presented an optimality-based model (Stocker and Prentice, 2024) which correctly predicts plant responses to both elevated  
702  $[\text{CO}_2]$  and N fertilisation, which could form the basis for including N limitation on plants in vegetation models on a sounder  
703 theoretical footing. However, a simpler and more pragmatic approach for including N limitation in LPJ-GUESS could be to  
704 constrain the formation of new leaf biomass based on the N that is available to fulfil the optimal stoichiometry of the new  
705 tissue (Smith et al., 2014). This optimal stoichiometry could be determined based on EEO-derived relationships which predict



706 leaf mass per unit area (LMA) purely from climatic growing conditions (Dong et al., 2023; Wang et al., 2023) and leaf N from  
707 LMA and  $V_{\text{cmax},25}$  (Dong et al., 2022). In such a framework the existing LPJ-GUESS formulations for N uptake and other  
708 aspects of the N cycle could be maintained. Even though the results here suggest that N limitation of GPP might be less  
709 important than previously thought, this topic deserves further attention in the future. In the meantime, removing the direct  
710 dependence of  $V_{\text{cmax}}$  on available N uncouples photosynthesis from the N cycle, and thus removes the dependence of  
711 photosynthesis on many uncertain input datasets, parameters, and processes involved in the N cycle, such as deposition data,  
712 soil decomposition, optimal C:N ratios, soil leaching, and translocation. The result is a simpler and more robust model which,  
713 as we have seen above, gives better GPP predictions.

714

#### 715 **4.6 Study limitations and outlook**

716 We have combined the standard daily climate input used in LPJ-GUESS with an explicit 15-day acclimation period. This  
717 configuration deviates from the subdaily P-model (Mengoli et al., 2022) in two ways: 1. the model acclimates to daily mean  
718 conditions and not noontime conditions, and 2. the model uses a single daily time step to calculate the fast response and actual  
719 photosynthetic rates rather than resolving the diurnal cycle. We have not quantified how far these approximations degrade  
720 model performance compared to the full subdaily implementation. This could be investigated in a future study. Alternatively,  
721 LPJ-GUESS could be adapted to use a subdaily timestep, as has already been done in a version of LPJ-GUESS modified to  
722 function as an LSM (Martín Belda et al., 2022) and maybe also be useful in the context of several coupled models involving  
723 LPJ-GUESS (Döscher et al., 2022; Forrest et al., 2020; Weiss et al., 2014). Adopting the full subdaily model is comparatively  
724 easy with the current implementation if the subdaily data is available, it is only necessary to use noontime climate variables  
725 when calculating  $V_{\text{cmax,opt}}$ ,  $J_{\text{max,opt}}$  and  $\xi_{\text{opt}}$  and subdaily (e.g. hourly) values for calculating  $V_{\text{cmax,indiv}}$ ,  $J_{\text{max,indiv}}$  and  $\xi_{\text{acclim}}$  at the  
726 subdaily timestep.

727

728 The simulations presented here focus exclusively on potential natural vegetation (PNV) and do not consider croplands, grazed  
729 lands or deforested areas. This results in a conceptual mismatch between the global evaluation data (GOSIF GPP data) and  
730 the LPJ-GUESS simulations. However, there are no major discrepancies between simulated and observed GPP in highly  
731 agricultural areas (for example in the Midwestern United States) or in grazing lands in either simulation, showing that both the  
732 standard and EEO versions of LPJ-GUESS captures GPP in anthropogenically modified landscapes reasonably well. The P-  
733 model has been successfully applied to simulate wheat yields globally (Qiao et al., 2021; Qiao et al., 2023; Qiao et al., 2026),  
734 so a full integration with LPJ-GUESS's land use functionality (Lindeskog et al., 2013, 2021) is likely a feasible further  
735 development. This would open the door to including such simulations into global carbon cycle initiatives such as the Global  
736 Carbon Project (Friedlingstein et al., 2023) and model intercomparison projects such as ISIMIP (Frieler et al., 2024).

737



738 We did not exclude FLUXNET sites that could potentially be affected by land use history or anthropogenic disturbance. This  
739 choice is reasonable given that we did not model these processes or prescribe PFTs abundances, and our intent was to evaluate  
740 performance globally, a scale at which implicitly includes a diverse array of land use and disturbance processes which causes  
741 deviations from PNV. Nevertheless, a more rigorous selection of test sites could improve the validation procedure.

## 742 **5 Conclusions**

743 We incorporated the P-model and a complementary representation of leaf dark respiration into the LPJ-GUESS DGVM. We  
744 tested this model configuration globally with full integration with the rest of LPJ-GUESS, i.e. with dynamic vegetation, fully  
745 prognostic fAPAR and leaf area index, and full coupling with hydrological cycle. Compared to the standard LPJ-GUESS  
746 version we saw moderate improvements in GPP patterns (both globally and at eddy flux covariance sites) accompanied by  
747 comparatively minimal impacts on the rest of the model functioning, as quantified by comparatively small (< 10%) changes  
748 in global carbon and water fluxes and pools, negligible change in global burnt area, and limited changes to the global biome  
749 distribution. Whilst we consider these improvements to be valuable in and of themselves (especially given that no tuning or  
750 calibration was applied), this approach brings other advantages, including: an embodiment of recent but well-validated theory  
751 which includes sensitivity to previously unconsidered drivers, namely VPD and atmospheric pressure; a reduced reliance on  
752 poorly-constrained PFT-specific parameters; decreased model run time; and better motivated scheme for plant water uptake.  
753 This work demonstrates the potential for EEO-derived theory to improve vegetation models, both as a general proof-of-concept  
754 and as specific, concrete first step for incorporating EEO theory into LPJ-GUESS.

## 755 **Appendices**

### 756 **Appendix A: Additional equations**

757 To preserve the flow of the main model description some standard formulations were omitted but are included here for  
758 completeness.

#### 759 **Appendix A1: Michaelis Menten coefficient**

760 The effective Michaelis-Menten coefficient for Rubisco kinetics,  $K(T)$ , was calculated as

$$761 K = K_c \cdot \left(1 + \frac{o}{K_o}\right) \quad (\text{A1})$$

762 where  $o$  is the atmospheric partial pressure of oxygen (pa) given by

$$763 o = [O_2] \cdot 10^{-6} \cdot p \quad (\text{A2})$$

764 and  $[O_2]$  is the mole fraction of oxygen taken as  $2.09476 \times 10^5$  ppm (parts per million).  $K_c$  and  $K_o$  are the Michaelis-Menten  
765 coefficients for carboxylation and oxygenation given by



766  $K_x = K_{x,25} \cdot f_{arrh}(T_K, \Delta H_a)$  (A3)

767 where  $x$  can denote either carboxylation ( $K_{c,25} = 39.97$  Pa,  $\Delta H_a = 79430$  J mol<sup>-1</sup>) or oxygenation ( $K_{o,25} = 27480$  Pa,  $\Delta H_a =$   
768 (Stocker et al., 2020)36380 J mol<sup>-1</sup>).

769

## 770 Appendix A2: Photorespiratory compensation point

771 The photorespiratory compensation point at a given temperature and pressure,  $\Gamma^*(T, p)$  is calculated by scaling from  $\Gamma^*_{25}$ , its  
772 value at 25°C and sea-level pressure (Bernacchi et al., 2001):

773

774 
$$\Gamma^*(T, p) = \Gamma^*_{25} \cdot f_r(T) \cdot \frac{p}{p_{sealevel}}$$
 (A4)

775

776 where  $\Gamma^*_{25} = 4.332$  Pa and  $f_r(T)$  the Arrhenius function with activation energy = 37830 J/mol.

## 777 Appendix A3: Intrinsic quantum yield of photosynthesis

778 The intrinsic quantum yield of photosynthesis,  $\varphi_0$ , is calculated separately for C3 (Bernacchi et al., 2003) and C4  
779 photosynthesis (Cai and Prentice, 2020).  $\widehat{C}_L$  is a calibratable parameter encompassing maximum quantum yield and leaf  
780 absorption properties, here set to 0.087182 following (Stocker et al., 2020).

781

782

783 
$$\varphi_{0,c3} = \widehat{C}_L \cdot \left( 0.352 + 0.022 \cdot T * - 3.4 \times 10^{-4} \cdot T^2 \right)$$
 (A5)

784 
$$\varphi_{0,c4} = \widehat{C}_L \cdot \left( -0.008 + 0.00375 \cdot T * - 0.58 \times 10^{-4} \cdot T^2 \right)$$
 (A6)

785

## 786 Appendix A4: Arrhenius function

787 When scaling variables to and from their values at 25°C, the normalised Arrhenius function (or its inverse) was used (Bernacchi  
788 et al., 2001)

789 
$$f_{arrh}(T_K, \Delta H_a) = e^{\left( \frac{\Delta H_a \cdot (T_K - T_{ref})}{R \cdot T_K \cdot T_{ref}} \right)}$$
 (A7)

790 where  $T_K$  is the temperature in Kelvin,  $T_{ref}$  is the reference temperature (298.15 K = 25 °C) and  $R$  is the universal gas constant  
791 (8.3145 J mol<sup>-1</sup> K<sup>-1</sup>) and  $\Delta H_a$  is the activation energy for the particular quantity.



792 **Appendix B: Additional tables**

793

IGBP Biome		Enabled PFTs
DBF	Deciduous broadleaved forest	TeBS, IBS, TrBR, TrIBR
EBF	Evergreen broadleaved forest	TeBE, TrBE, TrIBE
ENF	Evergreen needle-leaved forest	BNE, BINE, BNS, TeNE
MF	Mixed forest	All
OSH	Open shrubland	All
CSH	Closed shrubland	All
GRA	Grassland	C3G, C4G
SAV	Savanna	All
WSA	Woody savanna	All

794

795 **Table B1. IGBP biome types and enabled PFTs used in the LPJ-GUESS simulations of the FLUXNET2015 sites. The**  
 796 **full PFT set is: BNE - boreal needle-leaved evergreen tree, BINE - boreal shade-intolerant needle-leaved evergreen**  
 797 **tree, BNS - boreal needle-leaved summergreen tree, IBS - boreal/temperate shade intolerant broadleaved summergreen**  
 798 **tree, TeBS - temperate broadleaved summergreen tree, TeBE - temperate broadleaved evergreen tree, TrBE - tropical**  
 799 **broadleaved evergreen tree, TrIBE - tropical shade-intolerant broadleaved evergreen tree, TrBR - tropical**  
 800 **broadleaved raingreen tree, C3G - boreal/temperate C<sub>3</sub> photosynthesising grass, and C4G - tropical C<sub>4</sub>**  
 801 **photosynthesising grass.**



802

IGBP	Aggregation	N sites	$r^2$		RMSE	
			Standard	EEO	Standard	EEO
All	Daily	147	0.45	<b>0.48</b>	2.9	<b>2.8</b>
	5Day	147	0.45	<b>0.48</b>	2.7	2.7
	Monthly	147	0.55	<b>0.56</b>	<b>2.3</b>	2.4
CSH	Daily	2	<b>0.47</b>	0.35	1.9	1.9
	5Day	2	<b>0.54</b>	0.39	1.8	1.8
	Monthly	2	<b>0.65</b>	0.45	<b>1.5</b>	1.6
DBF	Daily	22	0.57	<b>0.6</b>	<b>3.1</b>	3.4
	5Day	22	0.56	<b>0.60</b>	<b>2.8</b>	3.4
	Monthly	22	0.64	<b>0.65</b>	<b>2.5</b>	3.2
EBF	Daily	13	<b>0.25</b>	0.22	<b>2.9</b>	3.2
	5Day	13	<b>0.31</b>	0.28	<b>2.6</b>	2.9
	Monthly	13	<b>0.42</b>	0.37	<b>2.3</b>	2.7
ENF	Daily	44	0.57	<b>0.58</b>	2.5	<b>2.3</b>
	5Day	44	0.56	<b>0.57</b>	<b>2.2</b>	2.3
	Monthly	44	0.64	<b>0.65</b>	<b>1.9</b>	2.1
GRA	Daily	32	0.35	<b>0.39</b>	3.5	<b>3.1</b>
	5Day	32	0.34	<b>0.39</b>	3.2	<b>2.9</b>
	Monthly	32	0.47	0.47	2.5	<b>2.4</b>
MF	Daily	10	0.54	<b>0.57</b>	2.7	2.7
	5Day	10	0.51	<b>0.54</b>	<b>2.5</b>	2.7
	Monthly	10	0.59	<b>0.61</b>	<b>2.2</b>	2.4
OSH	Daily	10	0.36	<b>0.41</b>	3.3	<b>2.4</b>
	5Day	10	0.34	<b>0.42</b>	3.1	<b>2.4</b>
	Monthly	10	0.45	<b>0.50</b>	3	<b>2.2</b>
SAV	Daily	8	0.29	<b>0.39</b>	2.7	<b>2.2</b>
	5Day	8	0.33	<b>0.42</b>	2.6	<b>2.3</b>
	Monthly	8	0.35	<b>0.48</b>	2.4	<b>2.1</b>
WSA	Daily	6	0.39	0.39	2.2	<b>2.1</b>
	5Day	6	0.46	0.46	<b>1.9</b>	2
	Monthly	6	0.52	<b>0.55</b>	<b>1.7</b>	1.9

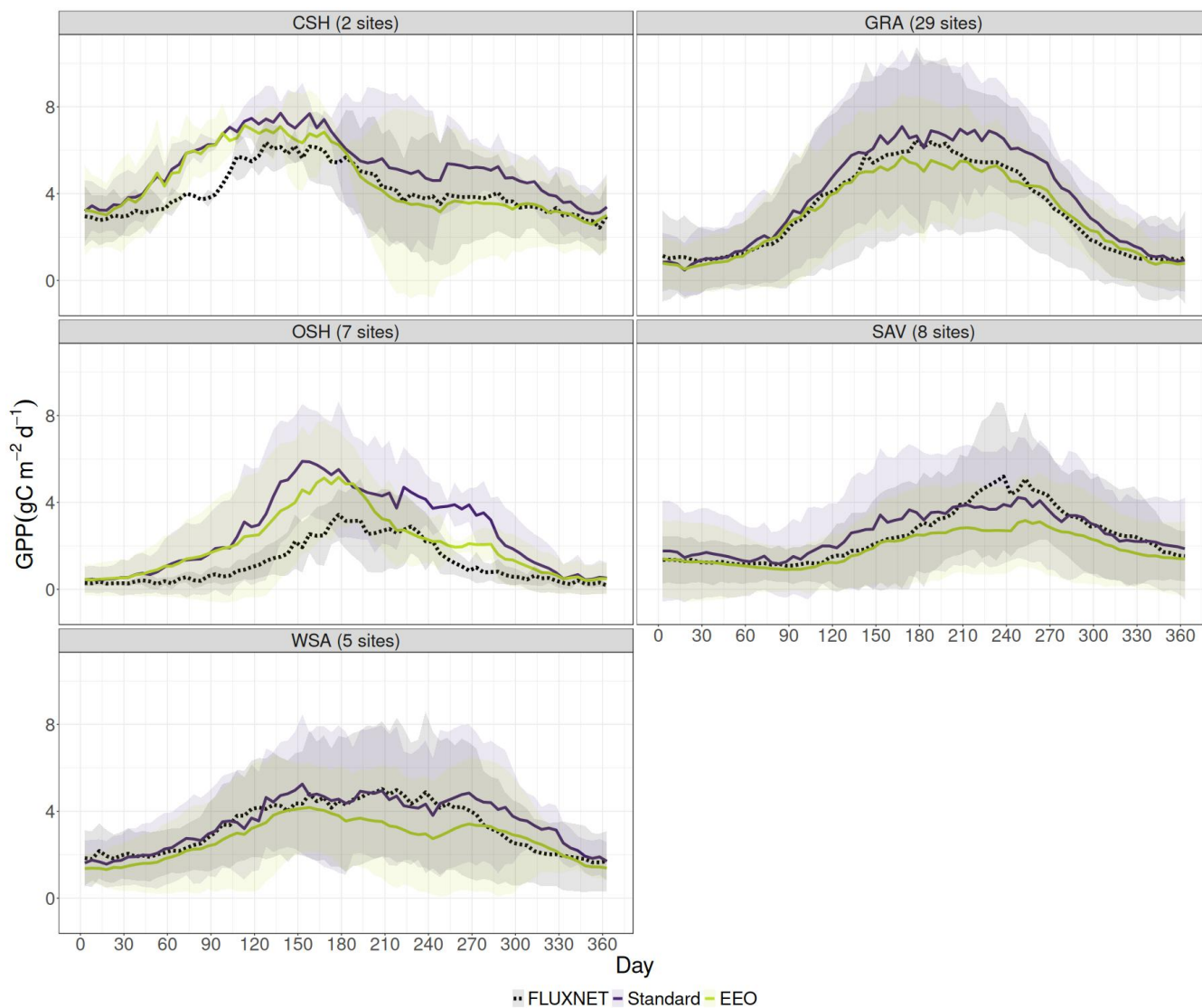
803

804 **Table B2. Coefficient of determination ( $r^2$ ) and root mean squared error (RMSE) for the LPJ-GUESS simulations**  
 805 **compared to FLUXNET2015 sites averaged across all sites and within the IGBP biome categorisation.**

806



807 **Appendix C: Additional figures**



808

809

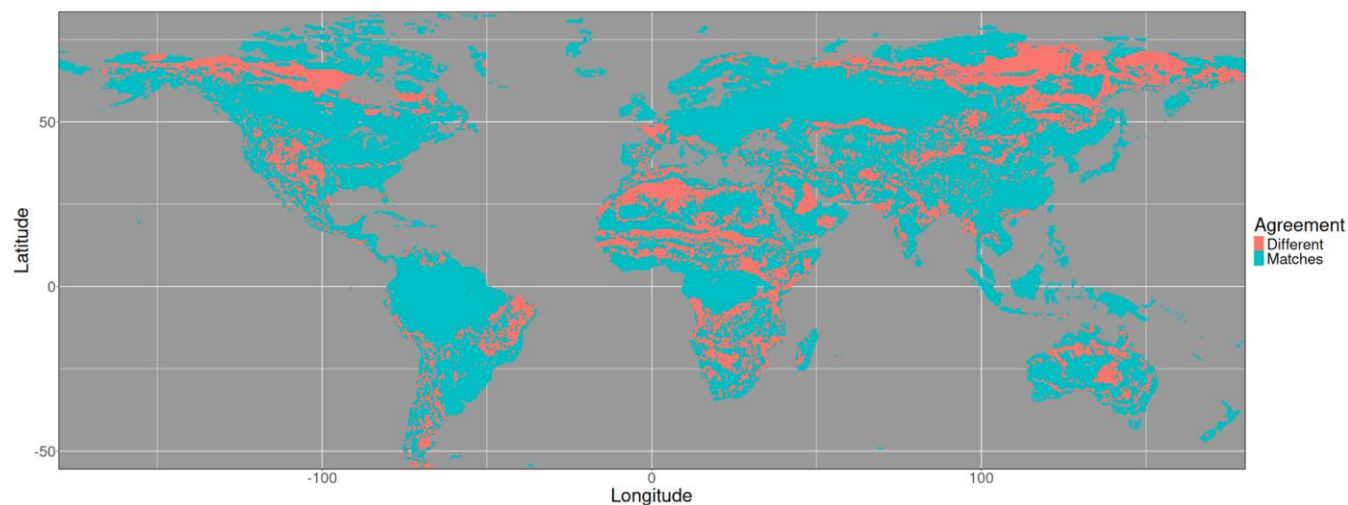
810

811

812

813

**Figure C1: Seasonal cycle of GPP from the LPJ-GUESS site simulations and the FLUXNET2015 data aggregated for closed shrublands (CSH), open shrublands (OSH), woody savannas (WSA), grasslands (GRA), and savannas (SAV).**



814

815 **Figure C2: Areas where the biome classifications match or differ between the *LPJ-GUESS Standard* and *LPJ-GUESS***  
816 ***EEO* simulation. Biomes as derived in Fig. 10.**

#### 817 **Code availability**

818 The LPJ-GUESS-EEO version used here (corresponding to git commit hash a3506d14 on the LPJ-GUESS developers  
819 repository) and the scripts for preparing input data, running simulations, and performing analyses and plotting are available at  
820 is available at the Zenodo repository Forrest (2026).

#### 821 **Data availability**

822 Outputs from the model simulations are available in the Zenodo repository Forrest (2026). The nitrogen deposition and the  
823 climate input data for the global simulations are available in the Zenodo repository Dantas de Paula (2024). The climate data  
824 for running the FLUXNET simulations are available from the Zenodo repository Gomes de Almeida (2026).

#### 825 **Author contribution**

826 MF and TH conceptualised the study, with contributions from MDdP, ICP and SH. MF designed the methodology and  
827 simulations, developed the software, conducted the investigation, performed the formal analysis, produced the visualisations,  
828 and prepared the initial version of the manuscript. FGdA produced the bias-corrected, gap-filled time series of climate data  
829 for the FLUXNET simulations. All authors contributed to the reviewing and editing of the final manuscript.



830 **Competing interests**

831 The authors declare that they have no conflict of interest.

832 **Acknowledgements**

833 This work used resources of the Deutsches Klimarechenzentrum (DKRZ) granted by its Scientific Steering Committee (WLA)  
834 under project ID 1202. This work is a contribution to the LEMONTREE (Land Ecosystem Models based On New Theory,  
835 obseRvations and ExperimEnts) project, supported by Schmidt Sciences (SPH, ICP). We thank Margot Knapen for her  
836 contribution of code for reading the FLUXNET data. We acknowledge and thank Jaideep Joshi and Guilia Mengoli for useful  
837 discussions.

838



839 **References**

840 **Anav, A., Friedlingstein, P., Beer, C., Ciais, P., Harper, A., Jones, C., Murray-Tortarolo, G., Papale, D., Parazoo, N.**  
841 **C., Peylin, P., Piao, S., Sitch, S., Viovy, N., Wiltshire, A., and Zhao, M.: Spatiotemporal patterns of terrestrial gross**  
842 **primary production: A review, *Reviews of Geophysics*, 53, 785–818, <https://doi.org/10.1002/2015RG000483>, 2015.**

843 **Arora, V. K., Katavouta, A., Williams, R. G., Jones, C. D., Brovkin, V., Friedlingstein, P., Schwinger, J., Bopp, L.,**  
844 **Boucher, O., Cadule, P., Chamberlain, M. A., Christian, J. R., Delire, C., Fisher, R. A., Hajima, T., Ilyina, T., Joetzjer,**  
845 **E., Kawamiya, M., Koven, C. D., Krasting, J. P., Law, R. M., Lawrence, D. M., Lenton, A., Lindsay, K., Pongratz, J.,**  
846 **Raddatz, T., Séférian, R., Tachiiri, K., Tjiputra, J. F., Wiltshire, A., Wu, T., and Ziehn, T.: Carbon–concentration and**  
847 **carbon–climate feedbacks in CMIP6 models and their comparison to CMIP5 models, *Biogeosciences*, 17, 4173–4222,**  
848 **<https://doi.org/10.5194/bg-17-4173-2020>, 2020.**

849 **Atkin, O. K., Evans, J. R., and Siebke, K.: Relationship between the inhibition of leaf respiration by light and**  
850 **enhancement of leaf dark respiration following light treatment, *Aust. J. Plant Physiol.*, 25, 437–443,**  
851 **<https://doi.org/10.1071/PP97159>, 1998.**

852 **Atkin, O. K., Bloomfield, K. J., Reich, P. B., Tjoelker, M. G., Asner, G. P., Bonal, D., Bönisch, G., Bradford, M. G.,**  
853 **Cernusak, L. A., Cosio, E. G., Creek, D., Crous, K. Y., Domingues, T. F., Dukes, J. S., Egerton, J. J. G., Evans, J. R.,**  
854 **Farquhar, G. D., Fyllas, N. M., Gauthier, P. P. G., Gloor, E., Gimeno, T. E., Griffin, K. L., Guerrieri, R., Heskell, M.**  
855 **A., Huntingford, C., Ishida, F. Y., Kattge, J., Lambers, H., Liddell, M. J., Lloyd, J., Lusk, C. H., Martin, R. E.,**  
856 **Maksimov, A. P., Maximov, T. C., Malhi, Y., Medlyn, B. E., Meir, P., Mercado, L. M., Mirotnick, N., Ng, D.,**  
857 **Niinemets, Ü., O’Sullivan, O. S., Phillips, O. L., Poorter, L., Poot, P., Prentice, I. C., Salinas, N., Rowland, L. M., Ryan,**  
858 **M. G., Sitch, S., Slot, M., Smith, N. G., Turnbull, M. H., VanderWel, M. C., Valladares, F., Veneklaas, E. J.,**  
859 **Weerasinghe, L. K., Wirth, C., Wright, I. J., Wythers, K. R., Xiang, J., Xiang, S., and Zaragoza-Castells, J.: Global**  
860 **variability in leaf respiration in relation to climate, plant functional types and leaf traits, *New Phytol.*, 206, 614–636,**  
861 **<https://doi.org/10.1111/nph.13253>, 2015.**

862 **Atkin, O. K., Bahar, N. H. A., Bloomfield, K. J., Griffin, K. L., Heskell, M. A., Huntingford, C., de la Torre, A. M., and**  
863 **Turnbull, M. H.: Leaf Respiration in Terrestrial Biosphere Models, in: *Plant Respiration: Metabolic Fluxes and***



- 864 **Carbon Balance**, edited by: Tcherkez, G. and Ghashghaie, J., Springer International Publishing, Cham, 107–142,  
865 [https://doi.org/10.1007/978-3-319-68703-2\\_6](https://doi.org/10.1007/978-3-319-68703-2_6), 2017.
- 866 **Bagley, J., Rosenthal, D. M., Ruiz-Vera, U. M., Siebers, M. H., Kumar, P., Ort, D. R., and Bernacchi, C. J.:** The  
867 **influence of photosynthetic acclimation to rising CO<sub>2</sub> and warmer temperatures on leaf and canopy photosynthesis**  
868 **models**, *Glob. Biogeochem. Cycles*, 29, 194–206, <https://doi.org/10.1002/2014GB004848>, 2015.
- 869 **Bernacchi, C. J., Singaas, E. L., Pimentel, C., Portis Jr, A. R., and Long, S. P.:** Improved temperature response  
870 **functions for models of Rubisco-limited photosynthesis**, *Plant Cell Environ.*, 24, 253–259,  
871 <https://doi.org/10.1111/j.1365-3040.2001.00668.x>, 2001.
- 872 **Bernacchi, C. J., Pimen<sup>TEL</sup>, C., and Long, S. P.:** In vivo temperature response functions of parameters required to model  
873 **RuBP-limited photosynthesis**, *Plant Cell Environ.*, 26, 1419–1430, <https://doi.org/10.1046/j.0016-8025.2003.01050.x>,  
874 2003.
- 875 **Bloomfield, K. J., Stocker, B. D., Keenan, T. F., and Prentice, I. C.:** Environmental controls on the light use efficiency  
876 **of terrestrial gross primary production**, *Glob. Change Biol.*, 29, 1037–1053, <https://doi.org/10.1111/gcb.16511>, 2023.
- 877 **Butler, E. E., Wythers, K. R., Flores-Moreno, H., Chen, M., Datta, A., Ricciuto, D. M., Atkin, O. K., Kattge, J.,**  
878 **Thornton, P. E., Banerjee, A., and Reich, P. B.:** Updated respiration routines alter spatio-temporal patterns of carbon  
879 **cycling in a global land surface model**, *Environ. Res. Lett.*, 16, 104015, <https://doi.org/10.1088/1748-9326/ac2528>, 2021.
- 880 **Cai, W. and Prentice, I. C.:** Recent trends in gross primary production and their drivers: analysis and modelling at  
881 **flux-site and global scales**, *Environ. Res. Lett.*, 15, 124050, <https://doi.org/10.1088/1748-9326/abc64e>, 2020.
- 882 **Chen, J.-L., Reynolds, J. F., Harley, P. C., and Tenhunen, J. D.:** Coordination theory of leaf nitrogen distribution in a  
883 **canopy**, *Oecologia*, 93, 63–69, <https://doi.org/10.1007/BF00321192>, 1993.
- 884 **Chen, R., Liu, L., Liu, X., and Rascher, U.:** CMLR: A Mechanistic Global GPP Dataset Derived from TROPOMIS SIF  
885 **Observations**, *J. Remote Sens.*, 4, 0127, <https://doi.org/10.34133/remotesensing.0127>, 2024.
- 886 **Collalti, A., Ibrom, A., Stockmarr, A., Cescatti, A., Alkama, R., Fernández-Martínez, M., Matteucci, G., Sitch, S.,**  
887 **Friedlingstein, P., Ciais, P., Goll, D. S., Nabel, J. E. M. S., Pongratz, J., Arneth, A., Haverd, V., and Prentice, I. C.:**



- 888 Forest production efficiency increases with growth temperature, *Nat. Commun.*, **11**, 5322,  
889 <https://doi.org/10.1038/s41467-020-19187-w>, 2020.
- 890 Collatz, G. J., Ball, J. T., Grivet, C., and Berry, J. A.: Physiological and environmental regulation of stomatal  
891 conductance, photosynthesis and transpiration: a model that includes a laminar boundary layer, *Agric. For. Meteorol.*,  
892 **54**, 107–136, [https://doi.org/10.1016/0168-1923\(91\)90002-8](https://doi.org/10.1016/0168-1923(91)90002-8), 1991.
- 893 Collatz, G. J., Ribas-Carbo, M., and Berry, J. A.: Coupled Photosynthesis-Stomatal Conductance Model for Leaves of  
894 C4 Plants, *Funct. Plant Biol.*, **19**, 519–538, <https://doi.org/10.1071/pp9920519>, 1992.
- 895 Crous, K. Y., Uddling, J., and De Kauwe, M. G.: Temperature responses of photosynthesis and respiration in evergreen  
896 trees from boreal to tropical latitudes, *New Phytol.*, **234**, 353–374, <https://doi.org/10.1111/nph.17951>, 2022.
- 897 Dantas de Paula, M.: LPJ-GUESS-CNP driver files, <https://doi.org/10.5281/zenodo.13472421>, 2024.
- 898 Dantas de Paula, M., Forrest, M., Warlind, D., Darela Filho, J. P., Fleischer, K., Rammig, A., and Hickler, T.: Including  
899 the phosphorus cycle into the LPJ-GUESS dynamic global vegetation model (v4.1, r10994) – global patterns and  
900 temporal trends of N and P primary production limitation, *Geosci. Model Dev.*, **18**, 2249–2274,  
901 <https://doi.org/10.5194/gmd-18-2249-2025>, 2025.
- 902 De Kauwe, M. G., Medlyn, B. E., Zaehle, S., Walker, A. P., Dietze, M. C., Wang, Y.-P., Luo, Y., Jain, A. K., El-Masri,  
903 B., Hickler, T., Wårlind, D., Weng, E., Parton, W. J., Thornton, P. E., Wang, S., Prentice, I. C., Asao, S., Smith, B.,  
904 McCarthy, H. R., Iversen, C. M., Hanson, P. J., Warren, J. M., Oren, R., and Norby, R. J.: Where does the carbon go?  
905 A model–data intercomparison of vegetation carbon allocation and turnover processes at two temperate forest free-air  
906 CO<sub>2</sub> enrichment sites, *New Phytol.*, **203**, 883–899, <https://doi.org/10.1111/nph.12847>, 2014.
- 907 Dong, N., Prentice, I. C., Wright, I. J., Wang, H., Atkin, O. K., Bloomfield, K. J., Domingues, T. F., Gleason, S. M.,  
908 Maire, V., Onoda, Y., Poorter, H., and Smith, N. G.: Leaf nitrogen from the perspective of optimal plant function, *J.*  
909 *Ecol.*, **110**, 2585–2602, <https://doi.org/10.1111/1365-2745.13967>, 2022.
- 910 Dong, N., Dechant, B., Wang, H., Wright, I. J., and Prentice, I. C.: Global leaf-trait mapping based on optimality theory,  
911 *Glob. Ecol. Biogeogr.*, **32**, 1152–1162, <https://doi.org/10.1111/geb.13680>, 2023.
- 912 Döscher, R., Acosta, M., Alessandri, A., Anthoni, P., Arsouze, T., Bergman, T., Bernardello, R., Boussetta, S., Caron,  
913 L.-P., Carver, G., Castrillo, M., Catalano, F., Cvijanovic, I., Davini, P., Dekker, E., Doblas-Reyes, F. J., Docquier, D.,  
914 Echevarria, P., Fladrich, U., Fuentes-Franco, R., Gröger, M., v. Hardenberg, J., Hieronymus, J., Karami, M. P.,  
915 Keskinen, J.-P., Koenigk, T., Makkonen, R., Massonnet, F., Ménégoz, M., Miller, P. A., Moreno-Chamarro, E.,  
916 Nieradzic, L., van Noije, T., Nolan, P., O’Donnell, D., Ollinaho, P., van den Oord, G., Ortega, P., Prims, O. T., Ramos,  
917 A., Reerink, T., Rousset, C., Ruprich-Robert, Y., Le Sager, P., Schmith, T., Schrödner, R., Serva, F., Sicardi, V., Sloth  
918 Madsen, M., Smith, B., Tian, T., Tourigny, E., Uotila, P., Vancoppenolle, M., Wang, S., Wårlind, D., Willén, U., Wyser,



- 919 **K., Yang, S., Yepes-Arbós, X., and Zhang, Q.:** The EC-Earth3 Earth system model for the Coupled Model  
920 **Intercomparison Project 6, Geosci. Model Dev., 15, 2973–3020, <https://doi.org/10.5194/gmd-15-2973-2022>, 2022.**
- 921 **Farquhar, G. D., von Caemmerer, S., and Berry, J. A.:** A biochemical model of photosynthetic CO<sub>2</sub> assimilation in  
922 **leaves of C<sub>3</sub> species, Planta, 149, 78–90, <https://doi.org/10.1007/BF00386231>, 1980.**
- 923 **Forrest, M., Tost, H., Lelieveld, J., and Hickler, T.:** Including vegetation dynamics in an atmospheric chemistry-enabled  
924 **general circulation model: linking LPJ-GUESS (v4.0) with the EMAC modelling system (v2.53), Geosci. Model Dev.,**  
925 **13, 1285–1309, <https://doi.org/10.5194/gmd-13-1285-2020>, 2020.**
- 926 **Forrest, M.:** Data and scripts for LPJ-GUESS-EEO model description paper. (submitted version - egusphere-2026-  
927 **3273), <https://doi.org/10.5281/zenodo.20589017>, 2026.**
- 928 **Friedlingstein, P., O’Sullivan, M., Jones, M. W., Andrew, R. M., Bakker, D. C. E., Hauck, J., Landschützer, P., Le**  
929 **Quéré, C., Luijkx, I. T., Peters, G. P., Peters, W., Pongratz, J., Schwingshackl, C., Sitch, S., Canadell, J. G., Ciais, P.,**  
930 **Jackson, R. B., Alin, S. R., Anthoni, P., Barbero, L., Bates, N. R., Becker, M., Bellouin, N., Decharme, B., Bopp, L.,**  
931 **Brasika, I. B. M., Cadule, P., Chamberlain, M. A., Chandra, N., Chau, T.-T.-T., Chevallier, F., Chini, L. P., Cronin,**  
932 **M., Dou, X., Enyo, K., Evans, W., Falk, S., Feely, R. A., Feng, L., Ford, D. J., Gasser, T., Ghattas, J., Gkritzalis, T.,**  
933 **Grassi, G., Gregor, L., Gruber, N., Gürses, Ö., Harris, I., Hefner, M., Heinke, J., Houghton, R. A., Hurtt, G. C., Iida,**  
934 **Y., Ilyina, T., Jacobson, A. R., Jain, A., Jarníková, T., Jersild, A., Jiang, F., Jin, Z., Joos, F., Kato, E., Keeling, R. F.,**  
935 **Kennedy, D., Klein Goldewijk, K., Knauer, J., Korsbakken, J. I., Körtzinger, A., Lan, X., Lefèvre, N., Li, H., Liu, J.,**  
936 **Liu, Z., Ma, L., Marland, G., Mayot, N., McGuire, P. C., McKinley, G. A., Meyer, G., Morgan, E. J., Munro, D. R.,**  
937 **Nakaoka, S.-I., Niwa, Y., O’Brien, K. M., Olsen, A., Omar, A. M., Ono, T., Paulsen, M., Pierrot, D., Pocock, K., Poulter,**  
938 **B., Powis, C. M., Rehder, G., Resplandy, L., Robertson, E., Rödenbeck, C., Rosan, T. M., Schwinger, J., Séférian, R.,**  
939 **et al.:** Global Carbon Budget 2023, *Earth Syst. Sci. Data*, 15, 5301–5369, <https://doi.org/10.5194/essd-15-5301-2023>,  
940 **2023.**
- 941 **Frieler, K., Volkholz, J., Lange, S., Schewe, J., Mengel, M., del Rocío Rivas López, M., Otto, C., Reyer, C. P. O., Karger,**  
942 **D. N., Malle, J. T., Treu, S., Menz, C., Blanchard, J. L., Harrison, C. S., Petrik, C. M., Eddy, T. D., Ortega-Cisneros,**  
943 **K., Novaglio, C., Rousseau, Y., Watson, R. A., Stock, C., Liu, X., Heneghan, R., Tittensor, D., Maury, O., Büchner, M.,**  
944 **Vogt, T., Wang, T., Sun, F., Sauer, I. J., Koch, J., Vanderkelen, I., Jägermeyr, J., Müller, C., Rabin, S., Klar, J., Vega**  
945 **del Valle, I. D., Lasslop, G., Chadburn, S., Burke, E., Gallego-Sala, A., Smith, N., Chang, J., Hantson, S., Burton, C.,**  
946 **Gädeke, A., Li, F., Gosling, S. N., Müller Schmied, H., Hattermann, F., Wang, J., Yao, F., Hickler, T., Marcé, R.,**  
947 **Pierson, D., Thiery, W., Mercado-Bettín, D., Ladwig, R., Ayala-Zamora, A. I., Forrest, M., and Bechtold, M.:** Scenario  
948 **setup and forcing data for impact model evaluation and impact attribution within the third round of the Inter-Sectoral**  
949 **Impact Model Intercomparison Project (ISIMIP3a), Geoscientific Model Development, 17, 1–51,**  
950 **<https://doi.org/10.5194/gmd-17-1-2024>, 2024.**



- 951 **Gerten, D., Schaphoff, S., Haberlandt, U., Lucht, W., and Sitch, S.: Terrestrial vegetation and water balance—**  
952 **hydrological evaluation of a dynamic global vegetation model, *J. Hydrol.*, 286, 249–270,**  
953 **<https://doi.org/10.1016/j.jhydrol.2003.09.029>, 2004.**
- 954 **Ghannoum, O., Caemmerer, S. von, Barlow, E. W. R., and Conroy, J. P.: The Effect of CO<sub>2</sub> Enrichment and Irradiance**  
955 **on the Growth, Morphology and Gas Exchange of a C<sub>3</sub> (*Panicum laxum*) and a C<sub>4</sub> (*Panicum antidotale*) Grass, *Aust.*  
956 ***J. Plant Physiol.*, 24, 227–237, <https://doi.org/10.1071/PP96077>, 1997.****
- 957 **Gomes de Almeida, F.: CRU-JRA v2.4 (1901 - 2022) climate data bias corrected with ICOS/FLUXNET sites data,**  
958 **<https://doi.org/10.5281/zenodo.20588381>, 2026.**
- 959 **Gu, L., Baldocchi, D. D., Wofsy, S. C., Munger, J. W., Michalsky, J. J., Urbanski, S. P., and Boden, T. A.: Response of**  
960 **a Deciduous Forest to the Mount Pinatubo Eruption: Enhanced Photosynthesis, *Science*, 299, 2035–2038,**  
961 **<https://doi.org/10.1126/science.1078366>, 2003.**
- 962 **Harrison, S. P., Cramer, W., Franklin, O., Prentice, I. C., Wang, H., Brännström, Å., de Boer, H., Dieckmann, U., Joshi,**  
963 **J., Keenan, T. F., Lavergne, A., Manzoni, S., Mengoli, G., Morfopoulos, C., Peñuelas, J., Pietsch, S., Rebel, K. T., Ryu,**  
964 **Y., Smith, N. G., Stocker, B. D., and Wright, I. J.: Eco-evolutionary optimality as a means to improve vegetation and**  
965 **land-surface models, *New Phytol.*, 231, 2125–2141, <https://doi.org/10.1111/nph.17558>, 2021.**
- 966 **Haverd, V., Smith, B., Nieradzik, L., Briggs, P. R., Woodgate, W., Trudinger, C. M., Canadell, J. G., and Cuntz, M.: A**  
967 **new version of the CABLE land surface model (Subversion revision r4601) incorporating land use and land cover**  
968 **change, woody vegetation demography, and a novel optimisation-based approach to plant coordination of**  
969 **photosynthesis, *Geosci. Model Dev.*, 11, 2995–3026, <https://doi.org/10.5194/gmd-11-2995-2018>, 2018.**
- 970 **Haxeltine, A. and Prentice, I. C.: A General Model for the Light-Use Efficiency of Primary Production, *Funct. Ecol.*,**  
971 **10, 551–561, <https://doi.org/10.2307/2390165>, 1996a.**
- 972 **Haxeltine, A. and Prentice, I. C.: BIOME3: An equilibrium terrestrial biosphere model based on ecophysiological**  
973 **constraints, resource availability, and competition among plant functional types, *Glob. Biogeochem. Cycles*, 10, 693–**  
974 **709, <https://doi.org/10.1029/96GB02344>, 1996b.**
- 975 **Hengl, T., Walsh, M. G., Sanderman, J., Wheeler, I., Harrison, S. P., and Prentice, I. C.: Global mapping of potential**  
976 **natural vegetation: an assessment of machine learning algorithms for estimating land potential, *PeerJ*, 6, e5457,**  
977 **<https://doi.org/10.7717/peerj.5457>, 2018.**
- 978 **Heskel, M. A., O’Sullivan, O. S., Reich, P. B., Tjoelker, M. G., Weerasinghe, L. K., Penillard, A., Egerton, J. J. G.,**  
979 **Creek, D., Bloomfield, K. J., Xiang, J., Sinca, F., Stangl, Z. R., Martinez-de la Torre, A., Griffin, K. L., Huntingford,**  
980 **C., Hurry, V., Meir, P., Turnbull, M. H., and Atkin, O. K.: Convergence in the temperature response of leaf respiration**



- 981 across biomes and plant functional types, *Proc. Natl. Acad. Sci.*, 113, 3832–3837,  
982 <https://doi.org/10.1073/pnas.1520282113>, 2016.
- 983 Hickler, T., Smith, B., Sykes, M. T., Davis, M. B., Sugita, S., and Walker, K.: Using a Generalized Vegetation Model to  
984 Simulate Vegetation Dynamics in Northeastern Usa, *Ecology*, 85, 519–530, <https://doi.org/10.1890/02-0344>, 2004.
- 985 Huber, M. L., Perkins, R. A., Laesecke, A., Friend, D. G., Sengers, J. V., Assael, M. J., Metaxa, I. N., Vogel, E., Mareš,  
986 R., and Miyagawa, K.: New International Formulation for the Viscosity of H<sub>2</sub>O, *J. Phys. Chem. Ref. Data*, 38, 101–  
987 125, <https://doi.org/10.1063/1.3088050>, 2009.
- 988 Huntingford, C., Atkin, O. K., Martinez-de la Torre, A., Mercado, L. M., Heskell, M. A., Harper, A. B., Bloomfield, K.  
989 J., O’Sullivan, O. S., Reich, P. B., Wythers, K. R., Butler, E. E., Chen, M., Griffin, K. L., Meir, P., Tjoelker, M. G.,  
990 Turnbull, M. H., Sitch, S., Wiltshire, A., and Malhi, Y.: Implications of improved representations of plant respiration  
991 in a changing climate, *Nat. Commun.*, 8, 1602, <https://doi.org/10.1038/s41467-017-01774-z>, 2017.
- 992 Intergovernmental Panel on Climate Change (IPCC) (Ed.): Global Carbon and Other Biogeochemical Cycles and  
993 Feedbacks, in: *Climate Change 2021 – The Physical Science Basis: Working Group I Contribution to the Sixth  
994 Assessment Report of the Intergovernmental Panel on Climate Change*, Cambridge University Press, Cambridge, 673–  
995 816, <https://doi.org/10.1017/9781009157896.007>, 2023.
- 996 Jeong, S., Ryu, Y., Gentine, P., Lian, X., Fang, J., Li, X., Dechant, B., Kong, J., Choi, W., Jiang, C., Keenan, T. F.,  
997 Harrison, S. P., and Prentice, I. C.: Persistent global greening over the last four decades using novel long-term



998 vegetation index data with enhanced temporal consistency, *Remote Sens. Environ.*, 311, 114282,  
999 <https://doi.org/10.1016/j.rse.2024.114282>, 2024.

1000 Kattge, J. and Knorr, W.: Temperature acclimation in a biochemical model of photosynthesis: a reanalysis of data  
1001 from 36 species, *Plant Cell Environ.*, 30, 1176–1190, <https://doi.org/10.1111/j.1365-3040.2007.01690.x>, 2007.

1002 Kelley, D. I., Prentice, I. C., Harrison, S. P., Wang, H., Simard, M., Fisher, J. B., and Willis, K. O.: A comprehensive  
1003 benchmarking system for evaluating global vegetation models, *Biogeosciences*, 10, 3313–3340,  
1004 <https://doi.org/10.5194/bg-10-3313-2013>, 2013.

1005 Klein Goldewijk, K., Beusen, A., and Janssen, P.: Long-term dynamic modeling of global population and built-up area  
1006 in a spatially explicit way: HYDE 3.1, *The Holocene*, 20, 565–573, <https://doi.org/10.1177/0959683609356587>, 2010.

1007 Knorr, W., Kaminski, T., Arneth, A., and Weber, U.: Impact of human population density on fire frequency at the  
1008 global scale, *Biogeosciences*, 11, 1085–1102, <https://doi.org/10.5194/bg-11-1085-2014>, 2014.

1009 Krinner, G., Viovy, N., de Noblet-Ducoudré, N., Ogée, J., Polcher, J., Friedlingstein, P., Ciais, P., Sitch, S., and Prentice,  
1010 I. C.: A dynamic global vegetation model for studies of the coupled atmosphere-biosphere system, *Glob. Biogeochem.*  
1011 *Cycles*, 19, <https://doi.org/10.1029/2003GB002199>, 2005.

1012 Kumarathunge, D. P., Medlyn, B. E., Drake, J. E., Tjoelker, M. G., Aspinwall, M. J., Battaglia, M., Cano, F. J., Carter,  
1013 K. R., Cavaleri, M. A., Cernusak, L. A., Chambers, J. Q., Crous, K. Y., De Kauwe, M. G., Dillaway, D. N., Dreyer, E.,  
1014 Ellsworth, D. S., Ghannoum, O., Han, Q., Hikosaka, K., Jensen, A. M., Kelly, J. W. G., Kruger, E. L., Mercado, L. M.,  
1015 Onoda, Y., Reich, P. B., Rogers, A., Slot, M., Smith, N. G., Tarvainen, L., Tissue, D. T., Togashi, H. F., Tribuzy, E. S.,  
1016 Uddling, J., Vårhammar, A., Wallin, G., Warren, J. M., and Way, D. A.: Acclimation and adaptation components of  
1017 the temperature dependence of plant photosynthesis at the global scale, *New Phytol.*, 222, 768–784,  
1018 <https://doi.org/10.1111/nph.15668>, 2019.

1019 Lamarque, J.-F., Dentener, F., McConnell, J., Ro, C.-U., Shaw, M., Vet, R., Bergmann, D., Cameron-Smith, P.,  
1020 Dalsoren, S., Doherty, R., Faluvegi, G., Ghan, S. J., Josse, B., Lee, Y. H., MacKenzie, I. A., Plummer, D., Shindell, D.  
1021 T., Skeie, R. B., Stevenson, D. S., Strode, S., Zeng, G., Curran, M., Dahl-Jensen, D., Das, S., Fritzsche, D., and Nolan,  
1022 M.: Multi-model mean nitrogen and sulfur deposition from the Atmospheric Chemistry and Climate Model



- 1023 **Intercomparison Project (ACCMIP): evaluation of historical and projected future changes, Atmos Chem Phys, 13,**  
1024 **7997–8018, <https://doi.org/10.5194/acp-13-7997-2013>, 2013.**
- 1025 **Lange, S.: Trend-preserving bias adjustment and statistical downscaling with ISIMIP3BASD (v1.0), Geosci. Model**  
1026 **Dev., 12, 3055–3070, <https://doi.org/10.5194/gmd-12-3055-2019>, 2019.**
- 1027 **Lapides, D. A., Hahm, W. J., Forrest, M., Rempe, D. M., Hickler, T., and Dralle, D. N.: Inclusion of bedrock vadose**  
1028 **zone in dynamic global vegetation models is key for simulating vegetation structure and function, Biogeosciences, 21,**  
1029 **1801–1826, <https://doi.org/10.5194/bg-21-1801-2024>, 2024.**
- 1030 **Li, X. and Xiao, J.: A Global, 0.05-Degree Product of Solar-Induced Chlorophyll Fluorescence Derived from OCO-2,**  
1031 **MODIS, and Reanalysis Data, Remote Sens., 11, 517, <https://doi.org/10.3390/rs11050517>, 2019.**
- 1032 **Li, Y., Zhou, L., Wang, S., Chi, Y., and Chen, J.: Leaf Temperature and Vapour Pressure Deficit (VPD) Driving**  
1033 **Stomatal Conductance and Biochemical Processes of Leaf Photosynthetic Rate in a Subtropical Evergreen Coniferous**  
1034 **Plantation, Sustainability, 10, 4063, <https://doi.org/10.3390/su10114063>, 2018.**
- 1035 **Liu, B., Wang, X., Liu, Q., Xu, Y., Arslan, A. M., Zheng, D., Li, L., and Gong, X.: Response of leaf day respiration in**  
1036 **C4 plants to irradiance and vapour pressure deficit, Crop Environ., 3, 101–111,**  
1037 **<https://doi.org/10.1016/j.crope.2023.12.001>, 2024.**
- 1038 **Maire, V., Martre, P., Kattge, J., Gastal, F., Esser, G., Fontaine, S., and Soussana, J.-F.: The Coordination of Leaf**  
1039 **Photosynthesis Links C and N Fluxes in C3 Plant Species, PLOS ONE, 7, e38345,**  
1040 **<https://doi.org/10.1371/journal.pone.0038345>, 2012.**
- 1041 **Martín Belda, D., Anthoni, P., Wårlind, D., Olin, S., Schurgers, G., Tang, J., Smith, B., and Arneth, A.: LPJ-**  
1042 **GUESS/LSMv1.0: a next-generation land surface model with high ecological realism, Geoscientific Model**  
1043 **Development, 15, 6709–6745, <https://doi.org/10.5194/gmd-15-6709-2022>, 2022.**



- 1044 **Medlyn, B. E., Duursma, R. A., Eamus, D., Ellsworth, D. S., Prentice, I. C., Barton, C. V. M., Crous, K. Y., De Angelis,**  
1045 **P., Freeman, M., and Wingate, L.: Reconciling the optimal and empirical approaches to modelling stomatal**  
1046 **conductance, *Glob. Change Biol.*, 17, 2134–2144, <https://doi.org/10.1111/j.1365-2486.2010.02375.x>, 2011.**
- 1047 **Mengoli, G., Agustí-Panareda, A., Boussetta, S., Harrison, S. P., Trotta, C., and Prentice, I. C.: Ecosystem**  
1048 **Photosynthesis in Land-Surface Models: A First-Principles Approach Incorporating Acclimation, *J. Adv. Model. Earth***  
1049 **Syst.**, 14, e2021MS002767, <https://doi.org/10.1029/2021MS002767>, 2022.
- 1050 **Mercado, L. M., Medlyn, B. E., Huntingford, C., Oliver, R. J., Clark, D. B., Sitch, S., Zelazowski, P., Kattge, J., Harper,**  
1051 **A. B., and Cox, P. M.: Large sensitivity in land carbon storage due to geographical and temporal variation in the**  
1052 **thermal response of photosynthetic capacity, *New Phytol.*, 218, 1462–1477, <https://doi.org/10.1111/nph.15100>, 2018.**
- 1053 **Middleby, K. B., Cheesman, A. W., and Cernusak, L. A.: Impacts of elevated temperature and vapour pressure deficit**  
1054 **on leaf gas exchange and plant growth across six tropical rainforest tree species, *New Phytol.*, 243, 648–661,**  
1055 **<https://doi.org/10.1111/nph.19822>, 2024.**
- 1056 **Miller, P. A. and Smith, B.: Modelling Tundra Vegetation Response to Recent Arctic Warming, *AMBIO*, 41, 281–291,**  
1057 **<https://doi.org/10.1007/s13280-012-0306-1>, 2012.**
- 1058 **Lindeskog, M., Arneeth, A., Bondeau, A., Waha, K., Seaquist, J., Olin, S., and Smith, B.: Implications of accounting for**  
1059 **land use in simulations of ecosystem carbon cycling in Africa, *Earth System Dynamics*, 4, 385–407,**  
1060 **<https://doi.org/10.5194/esd-4-385-2013>, 2013.**
- 1061 **Lindeskog, M., Smith, B., Lagergren, F., Sycheva, E., Ficko, A., Pretzsch, H., and Rammig, A.: Accounting for forest**  
1062 **management in the estimation of forest carbon balance using the dynamic vegetation model LPJ-GUESS (v4.0, r9710):**  
1063 **implementation and evaluation of simulations for Europe, *Geoscientific Model Development*, 14, 6071–6112,**  
1064 **<https://doi.org/10.5194/gmd-14-6071-2021>, 2021.**
- 1065 **Lombardozzi, D. L., Bonan, G. B., Smith, N. G., Dukes, J. S., and Fisher, R. A.: Temperature acclimation of**  
1066 **photosynthesis and respiration: A key uncertainty in the carbon cycle-climate feedback, *Geophysical Research Letters*,**  
1067 **42, 8624–8631, <https://doi.org/10.1002/2015GL065934>, 2015.**  
1068
- 1069 **Niu, G.-Y., Yang, Z.-L., Mitchell, K. E., Chen, F., Ek, M. B., Barlage, M., Kumar, A., Manning, K., Niyogi, D., Rosero,**  
1070 **E., Tewari, M., and Xia, Y.: The community Noah land surface model with multiparameterization options (Noah-MP):**



- 1071 **1. Model description and evaluation with local-scale measurements, *J. Geophys. Res. Atmospheres*, 116,**  
1072 **<https://doi.org/10.1029/2010JD015139>, 2011.**
- 1073 **Oliver, R. J., Mercado, L. M., Medlyn, B. E., Harris, P. P., and Clark, D. B.: Contrasting Impacts of Acclimation and**  
1074 **Adaptation of Photosynthetic Capacity to Temperature and CO<sub>2</sub> Across Biomes, *Glob. Biogeochem. Cycles*, 39,**  
1075 **e2024GB008398, <https://doi.org/10.1029/2024GB008398>, 2025.**
- 1076 **Parton, W. J., Scurlock, J. M. O., Ojima, D. S., Gilmanov, T. G., Scholes, R. J., Schimel, D. S., Kirchner, T., Menaut,**  
1077 **J.-C., Seastedt, T., Garcia Moya, E., Kamnalrut, A., and Kinyamario, J. I.: Observations and modeling of biomass and**  
1078 **soil organic matter dynamics for the grassland biome worldwide, *Glob. Biogeochem. Cycles*, 7, 785–809,**  
1079 **<https://doi.org/10.1029/93GB02042>, 1993.**
- 1080 **Pastorello, G., Trotta, C., Canfora, E., Chu, H., Christianson, D., Cheah, Y.-W., Poindexter, C., Chen, J., Elbashandy,**  
1081 **A., Humphrey, M., Isaac, P., Polidori, D., Reichstein, M., Ribeca, A., van Ingen, C., Vuichard, N., Zhang, L., Amiro,**  
1082 **B., Ammann, C., Arain, M. A., Ardö, J., Arkebauer, T., Arndt, S. K., Arriga, N., Aubinet, M., Aurela, M., Baldocchi,**  
1083 **D., Barr, A., Beamesderfer, E., Marchesini, L. B., Bergeron, O., Beringer, J., Bernhofer, C., Berveiller, D., Billesbach,**  
1084 **D., Black, T. A., Blanken, P. D., Bohrer, G., Boike, J., Bolstad, P. V., Bonal, D., Bonnefond, J.-M., Bowling, D. R.,**  
1085 **Bracho, R., Brodeur, J., Brümmer, C., Buchmann, N., Burban, B., Burns, S. P., Buysse, P., Cale, P., Cavagna, M.,**  
1086 **Cellier, P., Chen, S., Chini, I., Christensen, T. R., Cleverly, J., Collalti, A., Consalvo, C., Cook, B. D., Cook, D.,**  
1087 **Coursolle, C., Cremonese, E., Curtis, P. S., D’Andrea, E., da Rocha, H., Dai, X., Davis, K. J., Cinti, B. D., Grandcourt,**  
1088 **A. de Ligne, A. D., De Oliveira, R. C., Delpierre, N., Desai, A. R., Di Bella, C. M., Tommasi, P. di, Dolman, H., Domingo,**  
1089 **F., Dong, G., Dore, S., Duce, P., Dufréne, E., Dunn, A., Dušek, J., Eamus, D., Eichelmann, U., ElKhidir, H. A. M.,**  
1090 **Eugster, W., Ewenz, C. M., Ewers, B., Famulari, D., Fares, S., Feigenwinter, I., Feitz, A., Fensholt, R., Filippa, G.,**  
1091 **Fischer, M., Frank, J., Galvagno, M., et al.: The FLUXNET2015 dataset and the ONEFlux processing pipeline for eddy**  
1092 **covariance data, *Sci. Data*, 7, 225, <https://doi.org/10.1038/s41597-020-0534-3>, 2020.**
- 1093 **Peng, Y., Bloomfield, K. J., and Prentice, I. C.: A theory of plant function helps to explain leaf-trait and productivity**  
1094 **responses to elevation, *New Phytol.*, 226, 1274–1284, <https://doi.org/10.1111/nph.16447>, 2020.**
- 1095 **Peng, Y., Bloomfield, K. J., Cernusak, L. A., Domingues, T. F., and Colin Prentice, I.: Global climate and nutrient**  
1096 **controls of photosynthetic capacity, *Commun. Biol.*, 4, 462, <https://doi.org/10.1038/s42003-021-01985-7>, 2021.**
- 1097 **Piao, S., Sitch, S., Ciais, P., Friedlingstein, P., Peylin, P., Wang, X., Ahlström, A., Anav, A., Canadell, J. G., Cong, N.,**  
1098 **Huntingford, C., Jung, M., Levis, S., Levy, P. E., Li, J., Lin, X., Lomas, M. R., Lu, M., Luo, Y., Ma, Y., Myneni, R. B.,**  
1099 **Poulter, B., Sun, Z., Wang, T., Viovy, N., Zaehle, S., and Zeng, N.: Evaluation of terrestrial carbon cycle models for**



- 1100 their response to climate variability and to CO<sub>2</sub> trends, *Glob. Change Biol.*, **19**, 2117–2132,  
1101 <https://doi.org/10.1111/gcb.12187>, 2013.
- 1102 Prentice, I. C., Dong, N., Gleason, S. M., Maire, V., and Wright, I. J.: Balancing the costs of carbon gain and water  
1103 transport: testing a new theoretical framework for plant functional ecology, *Ecol. Lett.*, **17**, 82–91,  
1104 <https://doi.org/10.1111/ele.12211>, 2014.
- 1105 Prentice, I. C., Liang, X., Medlyn, B. E., and Wang, Y.-P.: Reliable, robust and realistic: the three R's of next-generation  
1106 land-surface modelling, *Atmospheric Chem. Phys.*, **15**, 5987–6005, <https://doi.org/10.5194/acp-15-5987-2015>, 2015.
- 1107 Qian, L., Yu, X., Zhang, Z., Wu, L., Fan, J., Xiang, Y., Chen, J., and Liu, X.: Assessing and improving the high  
1108 uncertainty of global gross primary productivity products based on deep learning under extreme climatic conditions,  
1109 *Sci. Total Environ.*, **957**, 177344, <https://doi.org/10.1016/j.scitotenv.2024.177344>, 2024.
- 1110 Qiao, S., Wang, H., Prentice, I. C., and Harrison, S. P.: Optimality-based modelling of climate impacts on global  
1111 potential wheat yield, *Environ. Res. Lett.*, **16**, 114013, <https://doi.org/10.1088/1748-9326/ac2e38>, 2021.
- 1112 Qiao, S., Harrison, S. P., Prentice, I. C., and Wang, H.: Optimality-based modelling of wheat sowing dates globally,  
1113 *Agricultural Systems*, **206**, 103608, <https://doi.org/10.1016/j.agsy.2023.103608>, 2023.
- 1114 Qiao, S., Harrison, S. P., Prentice, I. C., Huang, X., Wang, H., and Yu, C.: Adaptive Sowing Helps Mitigate Future  
1115 Wheat Losses Globally, *Earth's Future*, **14**, e2025EF006554, <https://doi.org/10.1029/2025EF006554>, 2026.
- 1116 Rabin, S. S., Melton, J. R., Lasslop, G., Bachelet, D., Forrest, M., Hantson, S., Kaplan, J. O., Li, F., Mangeon, S., Ward,  
1117 D. S., Yue, C., Arora, V. K., Hickler, T., Kloster, S., Knorr, W., Nieradzick, L., Spessa, A., Folberth, G. A., Sheehan, T.,  
1118 Voulgarakis, A., Kelley, D. I., Prentice, I. C., Sitch, S., Harrison, S., and Arneeth, A.: The Fire Modeling Intercomparison  
1119 Project (FireMIP), phase 1: experimental and analytical protocols with detailed model descriptions, *Geosci. Model  
1120 Dev.*, **10**, 1175–1197, <https://doi.org/10.5194/gmd-10-1175-2017>, 2017.
- 1121 Reich, P. B., Sendall, K. M., Stefanski, A., Wei, X., Rich, R. L., and Montgomery, R. A.: Boreal and temperate trees  
1122 show strong acclimation of respiration to warming, *Nature*, **531**, 633–636, <https://doi.org/10.1038/nature17142>, 2016.
- 1123 Reich, P. B., Stefanski, A., Rich, R. L., Sendall, K. M., Wei, X., Zhao, C., Hou, J., Montgomery, R. A., and Bermudez,  
1124 R.: Assessing the relevant time frame for temperature acclimation of leaf dark respiration: A test with 10 boreal and  
1125 temperate species, *Glob. Change Biol.*, **27**, 2945–2958, <https://doi.org/10.1111/gcb.15609>, 2021.
- 1126 Reichstein, M., Falge, E., Baldocchi, D., Papale, D., Aubinet, M., Berbigier, P., Bernhofer, C., Buchmann, N., Gilmanov,  
1127 T., Granier, A., Grünwald, T., Havránková, K., Ilvesniemi, H., Janous, D., Knohl, A., Laurila, T., Lohila, A., Loustau,  
1128 D., Matteucci, G., Meyers, T., Miglietta, F., Ourcival, J.-M., Pumpanen, J., Rambal, S., Rotenberg, E., Sanz, M.,  
1129 Tenhunen, J., Seufert, G., Vaccari, F., Vesala, T., Yakir, D., and Valentini, R.: On the separation of net ecosystem



- 1130 exchange into assimilation and ecosystem respiration: review and improved algorithm, *Glob. Change Biol.*, **11**, 1424–  
1131 1439, <https://doi.org/10.1111/j.1365-2486.2005.001002.x>, 2005.
- 1132 Ren, Y., Wang, H., Harrison, S. P., Prentice, I. C., Atkin, O. K., Smith, N. G., Mengoli, G., Stefanski, A., and Reich, P.  
1133 B.: Reduced global plant respiration due to the acclimation of leaf dark respiration coupled with photosynthesis, *New*  
1134 *Phytol.*, **241**, 578–591, <https://doi.org/10.1111/nph.19355>, 2024.
- 1135 Ren, Y., Wang, H., Harrison, S. P., Prentice, I. C., Mengoli, G., Zhao, L., Reich, P. B., and Yang, K.: Incorporating the  
1136 Acclimation of Photosynthesis and Leaf Respiration in the Noah-MP Land Surface Model: Model Development and  
1137 Evaluation, *J. Adv. Model. Earth Syst.*, **17**, e2024MS004599, <https://doi.org/10.1029/2024MS004599>, 2025.
- 1138 Sage, R. F., Sharkey, T. D., and Seemann, J. R.: Acclimation of Photosynthesis to Elevated CO<sub>2</sub> in Five C<sub>3</sub> Species I,  
1139 *Plant Physiol.*, **89**, 590–596, <https://doi.org/10.1104/pp.89.2.590>, 1989.
- 1140 Sellers, P. J., Berry, J. A., Collatz, G. J., Field, C. B., and Hall, F. G.: Canopy reflectance, photosynthesis, and  
1141 transpiration. III. A reanalysis using improved leaf models and a new canopy integration scheme., *Remote Sens.*  
1142 *Environ.*, **42**, 187–216, [https://doi.org/10.1016/0034-4257\(92\)90102-P](https://doi.org/10.1016/0034-4257(92)90102-P), 1992.
- 1143 Sitch, S., Smith, B., Prentice, I. C., Arneth, A., Bondeau, A., Cramer, W., Kaplan, J. O., Levis, S., Lucht, W., Sykes, M.  
1144 T., Thonicke, K., and Venevsky, S.: Evaluation of ecosystem dynamics, plant geography and terrestrial carbon cycling  
1145 in the LPJ dynamic global vegetation model, *Glob. Change Biol.*, **9**, 161–185, <https://doi.org/10.1046/j.1365-2486.2003.00569.x>, 2003.
- 1147 Smith, B., Prentice, I. C., and Sykes, M. T.: Representation of vegetation dynamics in the modelling of terrestrial  
1148 ecosystems: comparing two contrasting approaches within European climate space, *Glob. Ecol. Biogeogr.*, **10**, 621–637,  
1149 <https://doi.org/10.1046/j.1466-822X.2001.t01-1-00256.x>, 2001.
- 1150 Smith, B., Wårlind, D., Arneth, A., Hickler, T., Leadley, P., Siltberg, J., and Zaehle, S.: Implications of incorporating  
1151 N cycling and N limitations on primary production in an individual-based dynamic vegetation model, *Biogeosciences*,  
1152 **11**, 2027–2054, <https://doi.org/10.5194/bg-11-2027-2014>, 2014.
- 1153 Smith, N. G. and Dukes, J. S.: Plant respiration and photosynthesis in global-scale models: incorporating acclimation  
1154 to temperature and CO<sub>2</sub>, *Glob. Change Biol.*, **19**, 45–63, <https://doi.org/10.1111/j.1365-2486.2012.02797.x>, 2013.
- 1155 Smith, N. G., Keenan, T. F., Colin Prentice, I., Wang, H., Wright, I. J., Niinemets, Ü., Crous, K. Y., Domingues, T. F.,  
1156 Guerrieri, R., Yoko Ishida, F., Kattge, J., Kruger, E. L., Maire, V., Rogers, A., Serbin, S. P., Tarvainen, L., Togashi, H.



- 1157 **F., Townsend, P. A., Wang, M., Weerasinghe, L. K., and Zhou, S.-X.: Global photosynthetic capacity is optimized to**  
1158 **the environment, *Ecol. Lett.*, 22, 506–517, <https://doi.org/10.1111/ele.13210>, 2019.**
- 1159 **Spuler, F. R., Wessel, J. B., Comyn-Platt, E., Varnhell, J., and Cagnazzo, C.: ibicus: a new open-source Python package**  
1160 **and comprehensive interface for statistical bias adjustment and evaluation in climate modelling (v1.0.1), *Geosci. Model***  
1161 ***Dev.*, 17, 1249–1269, <https://doi.org/10.5194/gmd-17-1249-2024>, 2024.**
- 1162 **Stocker, B. D. and Prentice, I. C.: CN-model: A dynamic model for the coupled carbon and nitrogen cycles in terrestrial**  
1163 **ecosystems, <https://doi.org/10.1101/2024.04.25.591063>, 28 April 2024.**
- 1164 **Stocker, B. D., Wang, H., Smith, N. G., Harrison, S. P., Keenan, T. F., Sandoval, D., Davis, T., and Prentice, I. C.: P-**  
1165 **model v1.0: an optimality-based light use efficiency model for simulating ecosystem gross primary production, *Geosci.***  
1166 ***Model Dev.*, 13, 1545–1581, <https://doi.org/10.5194/gmd-13-1545-2020>, 2020.**
- 1167 **Stocker, B. D., Dong, N., Perkowski, E. A., Schneider, P. D., Xu, H., de Boer, H. J., Rebel, K. T., Smith, N. G., Van**  
1168 **Sundert, K., Wang, H., Jones, S. E., Prentice, I. C., and Harrison, S. P.: Empirical evidence and theoretical**  
1169 **understanding of ecosystem carbon and nitrogen cycle interactions, *New Phytol.*, 245, 49–68,**  
1170 **<https://doi.org/10.1111/nph.20178>, 2025.**
- 1171 **Tissue, D. T., Thomas, R. B., and Strain, B. R.: Long-term effects of elevated CO<sub>2</sub> and nutrients on photosynthesis and**  
1172 **rubisco in loblolly pine seedlings, *Plant Cell Environ.*, 16, 859–865, <https://doi.org/10.1111/j.1365-3040.1993.tb00508.x>,**  
1173 **1993.**
- 1174 **University of East Anglia Climatic Research Unit; Harris, I.C.: CRU JRA v2.4: A forcings dataset of gridded land**  
1175 **surface blend of Climatic Research Unit (CRU) and Japanese reanalysis (JRA) data; Jan.1901 - Dec.2022., NERC EDS**  
1176 **Centre for Environmental Data Analysis [dataset],**  
1177 **<https://catalogue.ceda.ac.uk/uuid/aed8e269513f446fb1b5d2512bb387ad>, 2023.**
- 1178 **Vuichard, N., Messina, P., Luysaert, S., Guenet, B., Zaehle, S., Ghattas, J., Bastrikov, V., and Peylin, P.: Accounting**  
1179 **for carbon and nitrogen interactions in the global terrestrial ecosystem model ORCHIDEE (trunk version, rev 4999):**  
1180 **multi-scale evaluation of gross primary production, *Geosci. Model Dev.*, 12, 4751–4779, [https://doi.org/10.5194/gmd-](https://doi.org/10.5194/gmd-12-4751-2019)**  
1181 **12-4751-2019, 2019.**
- 1182 **Walker, A. P., Beckerman, A. P., Gu, L., Kattge, J., Cernusak, L. A., Domingues, T. F., Scales, J. C., Wohlfahrt, G.,**  
1183 **Wullschlegel, S. D., and Woodward, F. I.: The relationship of leaf photosynthetic traits – V<sub>cmax</sub> and J<sub>max</sub> – to leaf**



- 1184 **nitrogen, leaf phosphorus, and specific leaf area: a meta-analysis and modeling study, *Ecol. Evol.*, 4, 3218–3235,**  
1185 **<https://doi.org/10.1002/ece3.1173>, 2014.**
- 1186 **Wang, H., Prentice, I. C., Keenan, T. F., Davis, T. W., Wright, I. J., Cornwell, W. K., Evans, B. J., and Peng, C.:**  
1187 **Towards a universal model for carbon dioxide uptake by plants, *Nat. Plants*, 3, 734–741, [https://doi.org/10.1038/s41477-](https://doi.org/10.1038/s41477-017-0006-8)**  
1188 **017-0006-8, 2017.**
- 1189 **Wang, H., Atkin, O. K., Keenan, T. F., Smith, N. G., Wright, I. J., Bloomfield, K. J., Kattge, J., Reich, P. B., and**  
1190 **Prentice, I. C.: Acclimation of leaf respiration consistent with optimal photosynthetic capacity, *Glob. Change Biol.*, 26,**  
1191 **2573–2583, <https://doi.org/10.1111/gcb.14980>, 2020.**
- 1192 **Wang, H., Prentice, I. C., Wright, I. J., Warton, D. I., Qiao, S., Xu, X., Zhou, J., Kikuzawa, K., and Stenseth, N. Chr.:**  
1193 **Leaf economics fundamentals explained by optimality principles, *Sci. Adv.*, 9, eadd5667,**  
1194 **<https://doi.org/10.1126/sciadv.add5667>, 2023.**
- 1195 **Weiss, M., Miller, P. A., van den Hurk, B. J. J. M., van Noije, T., Ștefănescu, S., Haarsma, R., van Ulft, L. H., Hazeleger,**  
1196 **W., Le Sager, P., Smith, B., and Schurgers, G.: Contribution of Dynamic Vegetation Phenology to Decadal Climate**  
1197 **Predictability, *J. Clim.*, 27, 8563–8577, <https://doi.org/10.1175/JCLI-D-13-00684.1>, 2014.**
- 1198 **Wolf, A., Callaghan, T. V., and Larson, K.: Future changes in vegetation and ecosystem function of the Barents Region,**  
1199 ***Clim. Change*, 87, 51–73, <https://doi.org/10.1007/s10584-007-9342-4>, 2008.**
- 1200 **Yang, J. C., Magney, T. S., Albert, L. P., Richardson, A. D., Frankenberg, C., Stutz, J., Grossmann, K., Burns, S. P.,**  
1201 **Syednasrollah, B., Blanken, P. D., and Bowling, D. R.: Gross primary production (GPP) and red solar induced**  
1202 **fluorescence (SIF) respond differently to light and seasonal environmental conditions in a subalpine conifer forest,**  
1203 ***Agric. For. Meteorol.*, 317, 108904, <https://doi.org/10.1016/j.agrformet.2022.108904>, 2022.**
- 1204 **Zhou, H., Tang, J., Olin, S., and Miller, P. A.: A comprehensive evaluation of hydrological processes in a second-**  
1205 **generation dynamic vegetation model, *Hydrol. Process.*, 38, e15152, <https://doi.org/10.1002/hyp.15152>, 2024.**